THESIS FOR THE DEGREE OF DOCTOR OF PHILOSOPHY IN SOLID AND
STRUCTURAL MECHANICS

Computational Homogenization of Mechanical and Electro-Chemical Properties in Structural Battery Electrolytes

VINH TU

Cover:
The figure shows an artificial 3D RVE based on SEM scan. The deformed pore space is marked in blue. The red arrows show how the ionic flux paths are affected as the microstructure is subjected to compression.

Computational Homogenization of Mechanical and Electro-Chemical Properties in Structural Battery Electrolytes
VINH TU
Department of Industrial and Materials Science
Division of Material and Computational Mechanics
Chalmers University of Technology

ABSTRACT

In the quest for weight efficient energy storage solutions, the structural battery is an emerging technology under development. It is a multifunctional composite material that can carry mechanical loads, and simultaneously store and release energy. This is made possible due to carbon fibers' ability to act not only as structural reinforcement materials, but also as electrode components. While conventional batteries rely solely on liquid electrolyte to allow for ion transfer between the electrodes, structural batteries exploit the so-called structural battery electrolyte (SBE). The SBE consists of two continuous phases; a solid polymer skeleton and a liquid electrolyte. The role of the liquid electrolyte is to allow for ion transfer, while the solid polymer skeleton provides load-bearing functionality. In short, the structural battery consists of carbon fibers (acting as electrodes) embedded in a porous SBE (electrolyte/matrix).

The first part of the thesis studies the multifunctional performance of various SBE microstructures by performing virtual material testing on numerically generated artificial Representative Volume Elements (RVEs). In particular, the effective ionic conductivity is obtained by solving a diffusion equation with Fick's law, and the effective stiffness by assuming linear elasticity. As a direct extension of this framework, coupled diffusion and large deformation in the SBE is also considered; i.e., ionic transport in an SBE subjected to mechanical loads using finite strain theory. Here, the aim is to compute the deformation-dependent effective mobility.

The second part covers the development of a multi-scale modeling framework for electro-chemically coupled ion transport in SBEs. After establishing the governing equations, Variationally Consistent Homogenization (VCH) is employed to obtain a two-scale model. If the sub-scale RVE problem exhibits negligible transient effects for length scales relevant to the studied application, then the assumption of micro-stationarity can be introduced. This opens up for the possibility to devise a numerically efficient solution scheme for the macro-scale problem that is based on a priori upscaling of the effective response.

Lastly, Numerical Model Reduction (NMR) is exploited to enable solution of fully transient electro-chemically coupled two-scale problems without assuming micro-stationarity. The goal is to exploit NMR by training a surrogate model, via Proper Orthogonal Decomposition (POD), that replaces the RVE simulations. The surrogate model takes the form of a system of Ordinary Differential Equations (ODE). The final NMR framework leads to a computationally efficient solution scheme for solving fully transient two-scale problems.

Keywords: FEM, Multi-scale Modeling, Computational Homogenization, Numerical Model Reduction, Multiphysics Modeling, Multifunctional Materials

May you be strengthened by yesterday's rain, walk straight in tomorrow's wind and cherish each moment of the sun today.

Preface

Acknowledgements

Thesis

This thesis consists of an extended summary and the following appended papers:

Paper A   **V. Tu**, L. E. Asp, N. Shirshova, F. Larsson, K. Runesson, and R. Jänicke. Performance of bicontinuous structural electrolytes. *Multifunctional Materials* **3** (2020), 025001.

Paper B   **V. Tu**, F. Larsson, K. Runesson, and R. Jänicke. Variationally consistent homogenization of electrochemical ion transport in a porous structural battery electrolyte. *European Journal of Mechanics - A/Solids* **98** (2023), 104901.

Paper C   **V. Tu**, F. Larsson, K. Runesson, and R. Jänicke. Numerical model reduction of multi-scale electrochemical ion transport. *To be submitted for publication.*

Paper D   **V. Tu**, F. Larsson, K. Runesson, and R. Jänicke. Deformation-dependent ionic transport in Structural Battery Electrolytes. *To be submitted for publication.*

The appended papers were prepared in collaboration with the co-authors. The author of this thesis was responsible for the major progress of the work in the papers, i.e. took part in formulating the theory, developed the numerical implementations, carried out the numerical simulations and prepared the manuscripts.

Other papers related to the thesis:

D. Carlstedt, K. Runesson, F. Larsson, **V. Tu**, R. Jänicke, and L. E. Asp. Computational modelling of structural batteries accounting for stress-assisted convection in the electrolyte. *International Journal of Solids and Structures* **238** (2022), 111343.

S. Duan, M. Cattaruzza, **V. Tu**, R. M. Auenhammer, R. Jänicke, M. K. G. Johansson, F. Liu, and L. E. Asp. Three-dimensional reconstruction and computational analysis of a structural battery composite electrolyte. *Communications Materials* **4** (2023), 49.

CONTENTS

Part I
Extended Summary

1 Introduction

Recent years have seen an upsurge in the vehicle electrification of road-based transportation [1]. The electric vehicle (EV) sales reached an all-time high of 14 million in 2023, representing nearly 18% of the global car sales [2]. There are various factors (demographic, technical, cost, governmental, psychological etc.) influencing consumers' willingness to purchase battery electric vehicles (BEVs) [3]. In the context of technical features, one of the largest technological barriers that is preventing consumers from purchasing BEVs is the limited driving range [3, 4]. Current solutions for battery packs face challenges with scalability as they are already heavy and bulky [5]. One way to improve this is by increasing the specific energy (Wh kg^{-1}) stored in the vehicle. Hence, there is a need for energy storage solutions that can provide significant system mass and volume savings in order to not only extend the driving range of EVs, but also improve other forms of sustainable transportation such as electric aviation [6].

1.1 Structural battery

Aside from further advancing existing electro-chemical energy storage technologies, an alternative strategy is to develop the so-called "structural battery". In contrast to conventional monofunctional batteries, the structural battery is multifunctional, enabling it to carry mechanical loads and simultaneously store and release energy [7, 8]. This technology relies on the carbon fiber's reversible lithium insertion capability [9] and its intrinsic ability to conduct current and carry tensile loads. Indeed, by fully utilizing all of the carbon fibers' capabilities, it becomes possible to exploit them as structural battery electrodes [10, 11]. Note here that it is only the negative electrodes that the carbon fibers can directly replace. One viable way to make the carbon fibers function as positive electrodes is to coat the fibers with lithium metal oxide or olivine based particles, e.g. LiFePO$_4$, binder and conductive additives [12–14].

While most conventional batteries[1] rely solely on liquid/gel electrolyte to allow for ion transfer between the electrodes, the structural battery exploits the so-called structural battery electrolyte (SBE) [15–17]. The SBE consists of two continuous phases; a nanoporous polymer skeleton and a liquid electrolyte. The role of the liquid electrolyte is to allow for ion transfer, while the porous polymer skeleton has load-bearing capability. In short, each constituent of the structural battery is designed to be multifunctional and utilized to its fullest potential; hence, ensuring that significant weight and volume savings are achieved [7, 8, 18].

---

[1]The only exception applies to solid-state batteries, which have solid electrolytes. However, large scale commercial solid-state batteries have yet to reach the market. Honda stated in 2022 that all-solid-state batteries might be deployed in 2024 [19], and Nissan also had a similar announcement targeting 2028 [20].
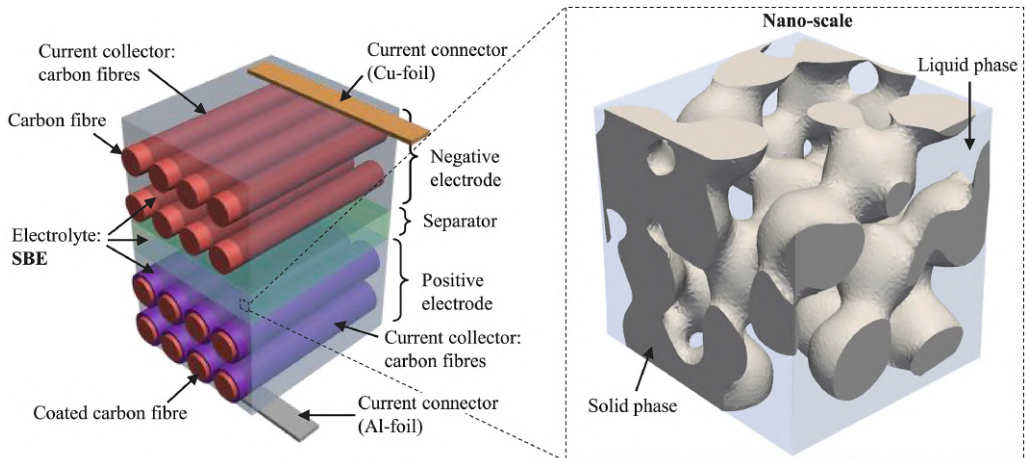
Figure 1.1: *Schematic illustration of the laminated structural battery (left image). Numerically generated artificial RVE (right image) representing the microstructure of the SBE that consists of a polymer skeleton and a liquid electrolyte. From Carlstedt et al. [32].*

So far, the most widespread structural battery architecture is the laminated version [7, 8], see Figure 1.1.

The complexity of structural batteries gives rise to numerous challenges that need to be overcome. A major challenge in producing high-performing structural batteries lies in the design and performance prediction of SBEs [7, 8]. In order to truly optimize the design w.r.t. the multifunctional performance, there is a need for modeling tools that can contribute to advancing SBE research.

Regarding research that has been performed in modeling of electro-chemical systems; Newman et al. was one of the first groups to develop numerical models of coupled electro-chemical reaction-diffusion in conventional batteries [21–23]. Additionally, we note the works by Samson et al. [24], Danilov and Notten [25], Dickinson et al. [26], and Bauer et al. [27] to name a few. Regarding multi-scale modeling of electro-chemical systems, we note that Salvadori and co-workers worked on the multi-scale analysis of electro-chemical systems [28, 29]. During recent years, modeling works related to structural batteries emerged. Xu et al. [30] performed multi-physics modeling of a single carbon fiber micro-battery. Carlstedt et al. [31–33] investigated structural battery modeling with emphasis on the multi-physics couplings, e.g. thermo–electro–chemo–mechanical and even accounted for stress-assisted convection in the SBE.

1.2 Research scope

Some of the existing battery research focuses on 1D single scale modeling, where the consideration of underlying microstructure effects are limited. Due to multi-physics phenomena (ion transport in nanoporous materials, electrode kinetics etc.) taking place several orders of magnitude below the battery cell size, it is clear that computational

modeling of batteries is inherently multi-scale in space and time [34]. As part of the long term goal of developing numerical models for structural batteries, this thesis aims at developing a multi-scale modeling[2] framework for Structural Battery Electrolytes (SBE). In order to achieve this, the following sub-goals are identified:

(i) Develop methods to numerically generate 3D Representative Volume Elements (RVEs) representing the SBE microstructures. This is addressed in **Paper A**.

(ii) Use virtual material tests to assess the performance of various SBE microstructures under different conditions. This topic is investigated in **Paper A** and **Paper D**.

(iii) Develop a multi-scale modeling framework for electro-chemically coupled ion transport in SBEs. Devise numerically efficient solution schemes to solve for two-scale problems. **Paper B** and **Paper C** are dedicated to this topic.

1.3 Limitations

The overarching theme in this thesis will be on the multi-scale modeling of SBEs. Here, we treat the SBE as a generic porous media in an electro-chemically coupled framework. The focus is put on method development and numerical modeling techniques. Hence, access to experimental validation will be limited. For studies focused on full battery modeling, see the related works on structural batteries by Carlstedt et al. [31–33] and Larsson et al. [35].

The artificial RVE generation in **Paper A** is performed with limited ability to enforce and predetermine certain microstructure features such as pore size distribution and tortuosity. Due to technical difficulties related to watertight geometry creation using the STL format, the artificial RVEs can in practice not be arbitrarily large. Moreover, the ion transport is modeled using Fick's law; hence, the more elaborate electro-chemical formulation involving both migration (caused by electric field) and diffusion of ions is not considered.

In **Paper B**, a rigorous treatment of electromagnetism (to properly resolve the electric field) would require involving Maxwell's equations, but by making the critical assumption that the magnetic field is assumed to vary slowly, the formulation is simplified to electrostatics. Additionally, the assumption of micro-stationarity is introduced in **Paper B** as a means to enable efficient two-scale modeling. However, this assumption hinges entirely on the fact that the transient effects are sufficiently small on the fine-scale.

The Numerical Model Reduction (NMR) in **Paper C** relies on POD to identify relevant modes to construct a surrogate model, which allows for numerically efficient solution of RVE problems. However, selecting optimal training data, training strategy and POD modes for maximum accuracy is challenging.

In **Paper D**, the empty pore space domain is modeled as a solid with a small fictitious stiffness to prevent self-penetration as the pore space is deformed. However, this assumption induces unwanted reaction forces between the solid and liquid domains.

---

[2]Although the mechanical (equilibrium) problem is scarcely treated in this thesis, the focus is still put on generic numerical methods and modeling techniques that are relevant for solid and structural mechanics.

1.4 Outline of thesis

Chapter 2 provides some additional background to Structural Electrolytes; it covers the manufacturing process and also existing experimental data. Based on the observed properties of real microstructures, a numerical RVE generation framework is developed. Chapter 3 focuses on virtual material testing via homogenization; in particular, the effective elastic stiffness and effective ionic conductivity are of interest. The chapter concludes with a study on the effective deformation-dependent mobility. Chapter 4 treats the topic of multi-scale modeling of electro-chemically coupled ionic transport in SBEs. Chapter 5 introduces the concept of Numerical Model Reduction (NMR) and applies it to RVE problems (direct continuation of Chapter 4) in order to decrease computational cost. Chapter 6 contains a brief summary of all appended papers. Finally, the conclusions from the research are presented in Chapter 7, together with an outlook for future developments.

2 Structural electrolytes

The structural battery is a type of structural power composite. Another innovation that also falls into this category is the structural supercapacitor, which shares the same challenges when it comes to the structural electrolyte; i.e. it is required to have high ionic conductivity while providing mechanical integrity [7]. In this section, we will consider structural electrolyte morphologies made for structural batteries as well as structural supercapacitors.

2.1 Synthesis

The two main methods for synthesis of (in-situ liquid filled) structural electrolytes are high internal phase emulsion (HIPE) templating [15] and polymerization induced phase separation (PIPS) [16, 17]. The HIPE templating approach mixes two immiscible phases to form an emulsion. Polymerization around emulsion droplets result in the formation of highly porous polymers. The PIPS method exploits components with specific solubility parameters. Initially, they might be fully miscible, but later on, they become immiscible as the monomers transform into polymers. Scanning electron microscope (SEM) images of several electrolyte systems based on both methods are shown in Figure 2.1.
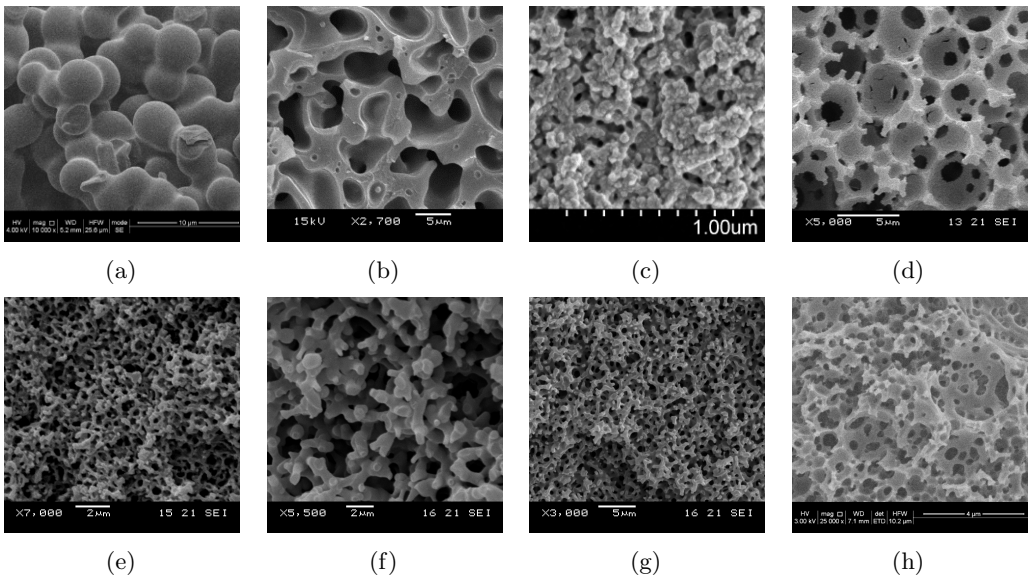
Figure 2.1: *SEM images of various structural electrolytes (solid polymer matrix); (a) 60DGEBA, (b) 50MTM57/2.3M_1PC, (c) AB/0.65, (d) polyHIPE, (e) 50VTM266/2.3M, (f) 30MVR444/2.3M, (g) 40MVR444/2.3M, and (h) polyMIPE. The names of the samples refer to their chemical composition and manufacturing method. Subfigure (c) from [16], rest from* **Paper A**.
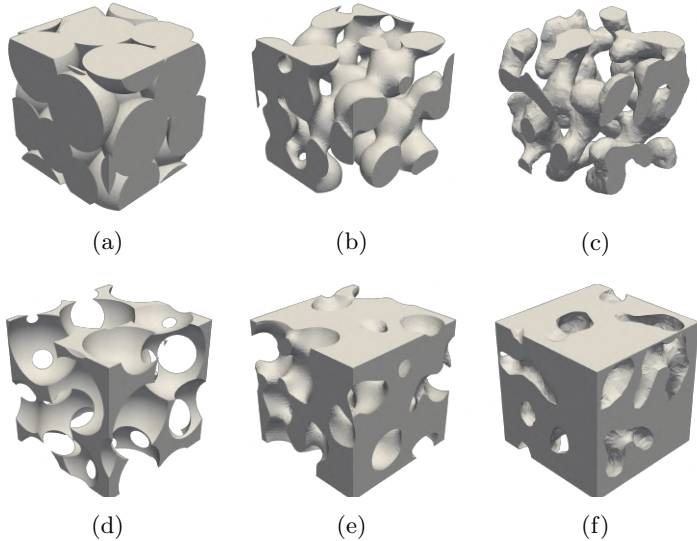
Figure 2.2: *Solid polymer matrix of various artificially generated microstructures; (a) bead, (b) trabecular, (c) imperfect trabecular, (d) inverse bead, (e) inverse trabecular, and (f) inverse imperfect trabecular.*

2.2 Artificial RVE generation

The Representative Volume Element (RVE) is a vital part of multi-scale modeling since it contains information of the underlying microstructure [36]. In a two-scale model, effective properties required for the macro-scale problem relies on the homogenization of the sub-scale RVE problem. Due to the complexity in obtaining and working with real 3D data of SBEs (e.g. from combined focused ion beam and SEM), an alternative approach is to numerically generate artificial RVEs for numerical analysis. This strategy is pursued in **Paper A**.

In this section, we attempt to generate some classes of periodic and bicontinuous microstructures that seem reasonable based on the collection of SEM images in Figure 2.1. Most of the generation techniques involve tampering with various Boundary Value Problems (BVP) to obtain solution fields that can be converted to meshable solids. An extensive overview on generation of random microstructures, with emphasis on bicontinuous mixtures, is available in Bargmann et al. [37, 38].

In this project, the following microstructure classes are generated:

(i) Bead structures: A dense sphere packing, with uniform particle size, is obtained by exploiting the Lubachevsky-Stillinger algorithm [39, 40]. In the next step, the radius is increased until the spheres overlap. The amount of overlap controls the porosity of the resulting structure within certain limits. The resulting 3D microstructures are porous and bicontinuous; resembling a structure built of sintered beads, see Figure 2.2a.

(ii) Trabecular structures: A periodic 3D Voronoi tesselation [41] with uniform cells is inserted into a smooth cube. The intersection of the Voronoi tesselation and the smooth cube results in periodic Voronoi cells enclosed in the cube. This is used as the input geometry for solving a fictitious linear stationary heat equation (in fact, any generic Poisson's equation) in the form as follows

$$\Delta\varphi = f \quad \text{in } \Omega, \tag{2.1}$$

where φ is a scalar field and f is a source term. Here, the edges of the Voronoi cells are constrained as heat sources, while the centers of the cells (seed points) are constrained as heat sinks. Additionally, periodic boundary conditions are exploited.

From the resulting 3D temperature distribution, isosurfaces at fixed temperature levels can (together with corresponding "isovolumes") be extracted and converted into meshable 3D solid structures, see Figure 2.2b. The final structures, denoted trabecular, are bicontinuous with interconnected pore channels. The porosity of the structure is controlled by varying the temperature level. The microstructure generation procedure is outlined in Figure 2.3.

(iii) Imperfect trabecular structures: This type of microstructure is obtained by solving the Cahn-Hilliard equation [42, 43] in the form as follows

$$\partial_t \phi + \boldsymbol{q}_\mu \cdot \boldsymbol{\nabla} = 0 \quad \text{in } \Omega, \tag{2.2}$$
$$(\phi^3 - \phi - \mu) + \boldsymbol{q}_\phi \cdot \boldsymbol{\nabla} = 0 \quad \text{in } \Omega, \tag{2.3}$$

with the constitutive relations

$$\boldsymbol{q}_\mu := -M\boldsymbol{\nabla}\mu, \tag{2.4}$$
$$\boldsymbol{q}_\phi := -\gamma\boldsymbol{\nabla}\phi. \tag{2.5}$$

where ϕ is the concentration difference between different phases, μ is the chemical potential, M is the mobility, and γ is related to the thickness of transition regions. Periodic boundary conditions are used.

These microstructures tend to be more irregular with pore channels that are not fully connected; the microstructure is only partly bicontinuous. There are both dead-end channels as well as some unconnected pores. Hence, we coin the name imperfect trabecular structures. The porosity of the imperfect trabecular structures is controlled by adjusting the magnitude of the initial condition to the Cahn-Hilliard equation. See Figure 2.4 for the microstructure generation procedure.

(iv) Inverted microstructures: Although this is not a truly distinct microstructure class, we reuse all microstructures by inverting them, see Figure 2.2d-2.2f. This results in the inverted bead structure, the inverted trabecular structure and the inverted imperfect trabecular structure.
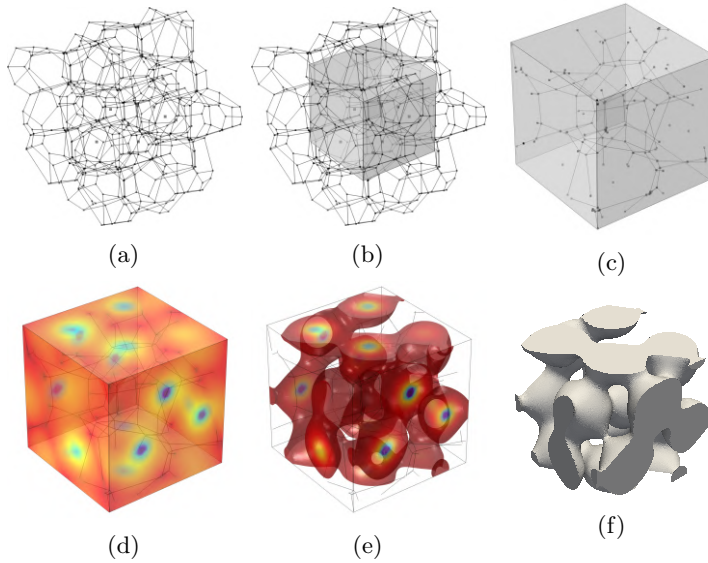
Figure 2.3: *Sequential steps for generation of trabecular structures; (a) periodic Voronoi tessellation, (b) embedding Voronoi tessellation in a cube, (c) constraints on a periodic network inside a cube, (d) temperature field of fictitious heat equation, (e) filtered temperature field, and (f) conversion to meshable solid.*
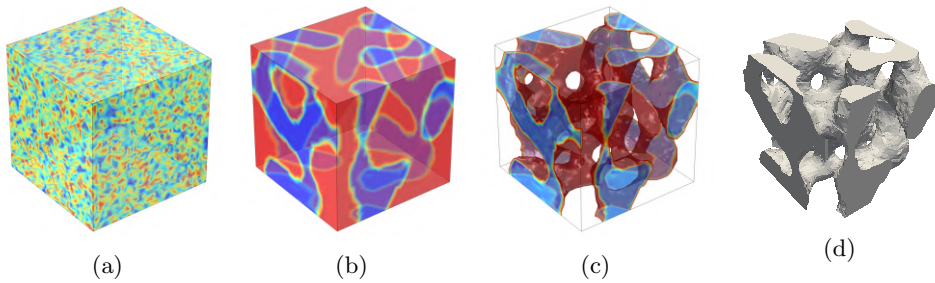
Figure 2.4: *Sequential steps for generation of imperfect trabecular structures; (a) noise distribution as initial condition, (b) solution field ϕ of Cahn-Hilliard equation, (c) filtered solution field, (d) conversion to meshable solid.*

3   Virtual material testing

In this section, virtual testing is exploited on the generated artificial microstructures to derive the effective material properties that characterize the macroscopic response. Here, we employ Computational Homogenization (CH), where the finite element method is used to solve for an RVE problem, see e.g. Geers et al. [44] and Miehe et al. [45]. For classical homogenization methods; see the works by Hill [36], Zohdi and Wriggers [46], and Nemat-Nasser and Hori [47] for mean-field and homogenization theories. While deriving effective material properties is a recurring method in **Paper A–D**; **Paper A** specifically focuses on linear and uncoupled problems, in particular linear elasticity and linear diffusion. Sub-scale quantities in the RVE domain $\Omega_\square$ are homogenized via the RVE volume averaging operator as follows

$$\langle \bullet \rangle_\square := \frac{1}{|\Omega_\square|} \int_{\Omega_\square} \bullet \; \mathrm{d}\Omega. \tag{3.1}$$

3.1   Elastic stiffness

In the simplest possible approach, the absence of pore pressure is assumed together with linear constitutive relations. This corresponds to characterizing mechanical properties of a drained microstructure (only solid phase $\Omega_{\square,\mathrm{S}}$). In the absence of body forces, linear elasticity on the sub-scale (with suitable boundary conditions) is defined as

$$-\boldsymbol{\sigma} \cdot \boldsymbol{\nabla} = \mathbf{0} \quad \text{in } \Omega_{\square,\mathrm{S}}, \tag{3.2a}$$

$$\boldsymbol{\sigma} = \mathbf{E} : \boldsymbol{\epsilon}, \tag{3.2b}$$

with the stress $\boldsymbol{\sigma}$, the strain $\boldsymbol{\epsilon}$, and the isotropic stiffness tensor $\mathbf{E}$ representing the (intrinsic) stiffness of the solid polymer phase. The elastic parameters in $\mathbf{E}$ are chosen as Young's modulus E and Poisson's ratio ν.

The goal is to compute the effective stiffness tensor $\bar{\mathbf{E}}$ of the porous solid phase via the macroscopic relation

$$\bar{\boldsymbol{\sigma}} = \bar{\mathbf{E}} : \bar{\boldsymbol{\epsilon}}, \tag{3.3}$$

with the effective strain $\bar{\boldsymbol{\epsilon}}$, and the (post-processed) effective stress $\bar{\boldsymbol{\sigma}} := \langle \boldsymbol{\sigma} \rangle_\square$ revealing the overall stiffness of the porous RVE.

Clearly, the sub-scale RVE problem needs to be solved in order to compute $\bar{\mathbf{E}}$. The first step is to introduce the classical assumption of first order homogenization as

$$\boldsymbol{u}(\boldsymbol{x}) = \bar{\boldsymbol{\epsilon}} \cdot \boldsymbol{x} + \boldsymbol{u}^{\mathrm{S}}(\boldsymbol{x}). \tag{3.4}$$

where $\boldsymbol{x}$ is the position in the RVE domain, $\boldsymbol{u}$ is the sub-scale displacement field, and $\boldsymbol{u}^{\mathrm{S}}$ is a periodic fluctuation field (from prescribing periodic boundary conditions) in the RVE. The macroscopic strain $\bar{\boldsymbol{\epsilon}}$ allows the macro-scale problem to interact with the sub-scale problem, and serves as the "input loading" to the RVE. Furthermore, note that a centered RVE is assumed, and that $\bar{\boldsymbol{u}} = \mathbf{0}$ since it simply represents a rigid body motion.

From here on, the sub-scale is solved by imposing the six independent loading cases of the symmetric macroscopic strain tensor $(\bar{\epsilon})_{kl}$ with $k, l = 1, 2, 3$. Finally, the components $(\bar{\mathsf{E}})_{ijkl}$ (with $i, j, k, l = 1, 2, 3$) of the macroscopic elasticity tensor can be computed from the macroscopic response $\langle (\boldsymbol{\sigma})_{ij} \rangle_{\square}$ of the RVE under the macroscopic unit strain $(\bar{\epsilon})_{kl} = 1$ via the relation

$$(\bar{\mathsf{E}})_{ijkl} = \frac{\partial \langle (\boldsymbol{\sigma})_{ij} \rangle_{\square}}{\partial (\bar{\epsilon})_{kl}} := \langle (\boldsymbol{\sigma})_{ij} \rangle_{\square} \Big|_{(\bar{\epsilon})_{kl}=1} . \tag{3.5}$$

3.2 Ionic conductivity

Under the assumption that chemical diffusion only occurs in the liquid electrolyte phase of the SBE $\Omega_{\square,\mathrm{E}}$, and that convection can be neglected; the linear stationary Fickian diffusion on the sub-scale (with suitable boundary conditions) is defined as

$$-\boldsymbol{j} \cdot \boldsymbol{\nabla} = 0 \quad \text{in } \Omega_{\square,\mathrm{E}}, \tag{3.6a}$$

$$\boldsymbol{j} := -M\, \boldsymbol{g}, \tag{3.6b}$$

where $\boldsymbol{j}$ is the ion mass flux, $\boldsymbol{g} := \boldsymbol{\nabla}\mu$ is the gradient of the chemical potential μ, and M is the intrinsic isotropic ionic conductivity of the liquid electrolyte.

In the same fashion as the elastic problem, the aim is to compute the effective ionic conductivity tensor $\bar{\boldsymbol{M}}$ via the macroscopic relation

$$\bar{\boldsymbol{j}} := -\bar{\boldsymbol{M}} \cdot \bar{\boldsymbol{g}}, \tag{3.7}$$

where $\bar{\boldsymbol{g}} := \boldsymbol{\nabla}\bar{\mu}$ and the effective (post-processed) ionic mass flux $\bar{\boldsymbol{j}} := \langle \boldsymbol{j} \rangle_{\square}$. Due to the heterogeneous distribution of the pore space in the RVE, $\bar{\boldsymbol{M}}$ might be anisotropic in contrast to the isotropic conductivity M of the liquid electrolyte.

Once again, first order homogenization is introduced as

$$\mu(\boldsymbol{x}) = \bar{\boldsymbol{g}} \cdot \boldsymbol{x} + \mu^{\mathrm{S}}(\boldsymbol{x}). \tag{3.8}$$

Finally, the sub-scale problem is solved by imposing the three independent loading cases of the gradient vector $(\bar{\boldsymbol{g}})_n$ with $n = 1, 2, 3$. The components $(\bar{\boldsymbol{M}})_{mn}$ (with $m, n = 1, 2, 3$) of the overall conductivity tensor can be computed from the RVE response $\langle (\boldsymbol{j})_m \rangle_{\square}$ of the RVE under the macroscopic unit gradient $(\bar{\boldsymbol{g}})_n = 1$ of the chemical potential via the relation

$$(\bar{\boldsymbol{M}})_{mn} = -\frac{\partial \langle (\boldsymbol{j})_m \rangle_{\square}}{\partial (\bar{\boldsymbol{g}})_n} := -\langle (\boldsymbol{j})_m \rangle_{\square} \Big|_{(\bar{\boldsymbol{g}})_n=1} . \tag{3.9}$$

Remark. The effective ionic conductivity computation can trivially be extended to include both chemical diffusion and ionic migration due to an electric field. The variable μ can simply be reinterpreted as the electro-chemical potential $\mu := \hat{\mu} + Fz\varphi$, where $\hat{\mu}$ is now the chemical potential and φ is the electric potential. Additionally, F is Faraday's constant and z is the charge number for e.g. Li-ions ($z = +1$). In fact, this holds even for the simplified balance equation (Fickian diffusion) since the effective ionic conductivity only depends on the sub-scale ionic flux $\boldsymbol{j} := -M\, \boldsymbol{g}$. Obviously, this holds true only upon making the critical model assumption that the electric potential does not need to be resolved in all domains. $\quad \square$

Quasi-isotropic properties

A limitation of the proposed artificial RVE generation technique lies in the limited RVE size and, therefore, the statistical representation of microstructure features. The computed effective stiffness tensors $\bar{\mathbf{E}}$ and ionic conductivity tensors $\bar{\mathbf{M}}$ might contain some anisotropy; hence, we compute quasi-isotropic scalar values for $\bar{E}$ and $\bar{M}$.

There are several ways to do this; however, in **Paper A**, the effective bulk modulus $\bar{K}$ and the effective shear modulus $\bar{G}$ are computed as follows

$$\bar{G} \quad := \quad \frac{1}{3}[(\bar{\mathbf{E}})_{1212} + (\bar{\mathbf{E}})_{1313} + (\bar{\mathbf{E}})_{2323}], \tag{3.10}$$

$$\bar{K} \quad := \quad \frac{1}{3}[(\bar{\mathbf{E}})_{1122} + (\bar{\mathbf{E}})_{1133} + (\bar{\mathbf{E}})_{2233}] + \frac{2}{3}\bar{G}. \tag{3.11}$$

In the next step, the quasi-isotropic Young's modulus is obtained as

$$\bar{E} = \frac{9\bar{K}\bar{G}}{3\bar{K} + \bar{G}}. \tag{3.12}$$

Finally, the quasi-isotropic ionic conductivity is computed as

$$\bar{M} := \frac{1}{3}[(\bar{\mathbf{M}})_{11} + (\bar{\mathbf{M}})_{22} + (\bar{\mathbf{M}})_{33}]. \tag{3.13}$$

3.3 Deformation-dependent ionic transport in SBE

Up to this point, we have only considered linear and uncoupled problems (**Paper A**). While this approach provides a simple and fast framework for evaluating and comparing the performance of various microstructures, it does not fully reflect the real operating conditions of an SBE. Under normal conditions, the structural battery is subjected to mechanical loads that will deform the pore space of the SBE, and potentially even cause blockages that might reduce the ionic transport. Hence, it is imperative to account for the pore space deformation during ionic transport in a non-linear and coupled fashion. Although no such numerical investigation has been performed specifically for SBEs, the problem at hand has many similarities to the broader topic of deformation-dependent diffusion.

Klepach and Zohdi [48] analyzed strongly-coupled deformation-dependent diffusion in composite media assuming finite strains. They considered the effects of deformation and accounted for it by incorporating it in the diffusivity tensor. More specifically, they formulated a diffusivity tensor that depends on the volumetric strain via $J = \det(\boldsymbol{F})$. For elasticity, they employed a Kirchhoff–Saint Venant material. Voges et al. [49] investigated deformation dependency of the (local/fine-scale) diffusion flux in solids at large deformations. In particular, they compared the assumption of isotropy of the mobility tensor in (i) the current configuration vs. (ii) the reference configuration.

These were a few examples of similar works, but none of them address the deformation-dependency of ionic transport that stems from deforming microstructures with complex morphology. In other words, there is a lack of understanding of how the effective ionic

transport properties are affected by microstructure deformation. In **Paper D**, we consider the coupled and geometrically non-linear extension; i.e. we model the ionic transport in an SBE subjected to mechanical loads using finite strain theory. Exploiting the same computational homogenization framework and artificial microstructures as before, we are now interested in computing the deformation-dependent effective mobility[1].

In the first step, we solve the the mechanical (equilibrium) problem under macro-scale deformation control, while adopting Neo-Hooke hyperelasticity for the fine-scale modeling of the solid skeleton. Assuming that experimental data for the effective mechanical response are available, the fine-scale elastic material parameters can be calibrated against macro-scale data.

With the pore space displacement field at hand, we can now compute the deformation-dependent effective mobility. The is achieved by solving for mass balance/diffusion with a Fickian constitutive relation and a constant mobility in the deformed configuration. Pull-back to the undeformed configuration then gives the pertinent deformation dependent mobility for the fine-scale model. In the final step, we apply computational homogenization to obtain the effective mobility pertaining to the macro-scale chemical potential gradient.

Balance equations

The mechanical problem reads: Find $\boldsymbol{u} : \Omega \to \mathbb{R}^3$ that solves the equilibrium equation with boundary conditions

$$-\boldsymbol{P} \cdot \boldsymbol{\nabla}_X = \boldsymbol{0} \quad \text{in } \Omega, \tag{3.14a}$$

$$\boldsymbol{u} = \boldsymbol{u}^{\mathrm{p}} \quad \text{on } \Gamma_{\mathrm{D}}^{(u)}, \tag{3.14b}$$

$$\boldsymbol{t}_X = \boldsymbol{P} \cdot \boldsymbol{N} = \boldsymbol{t}_X^{\mathrm{p}} \quad \text{on } \Gamma_{\mathrm{N}}^{(u)}, \tag{3.14c}$$

which represents a solvable system when complemented with suitable constitutive relations. Here, $\boldsymbol{P}$ is the first Piola–Kirchhoff stress tensor. The equilibrium equation is valid on the entire domain $\Omega = \Omega_{\mathrm{S}} \cup \Omega_{\mathrm{E}}$.

We assume that the SBE is drained during mechanical loading, indicating that liquid pressure inside the pore system Ω_{E} can be ignored. In other words, the liquid electrolyte does not contribute to the mechanical response of the microstructure in this model. However, in order to compute the deformation-dependent mobility (via an ionic transport problem in Lagrangian formulation), it is crucial to know how much the pore space deforms. This can be achieved by modeling the liquid electrolyte domain Ω_{E} as a solid with a small fictitious stiffness, whereby mechanically loading the microstructure will lead to deformations in Ω_{E} without introducing any significant reaction forces acting on Ω_{S}. Additionally, we also do this as a way to enable "contact" by requiring the volume of the pore space to be non-negative during compression; in other words, we prevent self-penetration of the solid polymer phase.

---

[1]The previous property of interest for ionic transport (in the previous section) was the ionic conductivity, but we shall now consider the ionic mobility. Both are modeled in the same fashion using a linear Fickian type of constitutive relation; the only difference now is that their effective properties depend on respective intrinsic parameter. In practice, the distinction lies only in the terminology used.

The next step is to analyze the ionic transport, which is modeled as a "diffusion problem". Mass balance, in the deformed format, for a single diffusing species in the deformed pore space ω_{E} reads

$$\boldsymbol{j} \cdot \boldsymbol{\nabla} = 0 \quad \text{in } \omega_{\mathrm{E}}. \tag{3.15}$$

Next, performing pull-back, the material format leads to the following problem: Find the chemical potential $\mu : \Omega_{\mathrm{E}} \to \mathbb{R}$, such that

$$\boldsymbol{J} \cdot \boldsymbol{\nabla}_X = 0 \quad \text{in } \Omega_{\mathrm{E}}. \tag{3.16a}$$

$$\mu = \mu^{\mathrm{p}} \quad \text{on } \Gamma_{\mathrm{D}}^{(\mu)}, \tag{3.16b}$$

$$J_N := \boldsymbol{J} \cdot \boldsymbol{N} = J^{\mathrm{p}} \quad \text{on } \Gamma_{\mathrm{N}}^{(\mu)}, \tag{3.16c}$$

$$J_N = 0 \quad \text{on } \Gamma_{\mathrm{S/E}}, \tag{3.16d}$$

when complemented with the constitutive relations defined below. Here, $\boldsymbol{J}$ is the molar (ionic) flux. Eq. (3.16a) is valid only in the electrolyte domain Ω_{E}, whose boundary is decomposed as $\partial \Omega_{\mathrm{E}} = \Gamma_{\mathrm{D}}^{(\mu)} \cup \Gamma_{\mathrm{N}}^{(\mu)} \cup \Gamma_{\mathrm{S/E}}$. This means that the ionic transport process inside the solid domain Ω_{S} is assumed to be negligible. Additionally, Eq. (3.16d) is used to prohibit ion transport through the solid-electrolyte interface $\Gamma_{\mathrm{S/E}} = \partial \Omega_{\mathrm{S}} \cap \partial \Omega_{\mathrm{E}}$.

Constitutive relations

A compressible version Neo-Hooke hyperelasticity [50] is assumed for the fine-scale modeling of the solid skeleton. The volume specific strain energy density Ψ reads as follows

$$\Psi(\boldsymbol{C}) = \frac{G}{2} \left[\mathrm{tr}(\boldsymbol{C}) - 3 \right] - G \ln(J) + \frac{\lambda}{2} \ln(J)^2, \tag{3.17a}$$

$$\boldsymbol{S}(\boldsymbol{C}) = 2 \frac{\partial \Psi}{\partial \boldsymbol{C}} = G \left[\boldsymbol{I} - \boldsymbol{C}^{-1} \right] + \lambda \ln(J) \, \boldsymbol{C}^{-1}, \tag{3.17b}$$

where λ and G are the elastic Lamé parameters. Further, $\boldsymbol{C} = \boldsymbol{F}^T \cdot \boldsymbol{F}$ is the right Cauchy-Green deformation tensor. Here, $\boldsymbol{F} = \boldsymbol{I} + \boldsymbol{u} \otimes \boldsymbol{\nabla}_X$ is the deformation gradient, and $J = \det(\boldsymbol{F})$ is the relative volume change. Lastly, $\boldsymbol{S}$ is the 2nd Piola-Kirchhoff stress that is used to compute the 1st Piola-Kirchhoff stress as an explicit function of the deformation gradient: $\boldsymbol{P}(\boldsymbol{F}) = \boldsymbol{F} \cdot \boldsymbol{S}(\boldsymbol{F}^T \cdot \boldsymbol{F})$.

As previously mentioned, we need to model the liquid electrolyte phase as a solid with a small fictitious stiffness in order to define a deformation map in the pore space Ω_{E}. Hence, we assume Neo-Hooke hyperelasticity also in the liquid domain. Note that for any finite value of λ, the Neo-Hooke model in (3.17a) will enforce $J > 0$. Hence, even for a small fictitious stiffness, the pore space will prevent penetration of the solid constituents.

For ionic transport, we assume mass balance/diffusion with a Fickian constitutive relation and a constant mobility. In the deformed configuration, the constitutive model reads

$$\boldsymbol{j} = -\boldsymbol{m} \cdot \boldsymbol{g}, \tag{3.18}$$

where $\boldsymbol{m}$ is the intrinsic fine-scale mobility tensor of the considered ionic species and $\boldsymbol{g} := \boldsymbol{\nabla}\mu$. A pull-back to the undeformed configuration gives the ionic Piola-flux

$$\boldsymbol{J}(\boldsymbol{F}, \boldsymbol{G}) = J\boldsymbol{F}^{-1} \cdot \boldsymbol{j} = -\boldsymbol{M}(\boldsymbol{F}) \cdot \boldsymbol{G}, \tag{3.19}$$

with

$$\boldsymbol{M}(\boldsymbol{F}) = J\boldsymbol{F}^{-1} \cdot \boldsymbol{m} \cdot \boldsymbol{F}^{-T}, \tag{3.20}$$

representing the fine-scale mobility in Lagrangian setting and $\boldsymbol{G} := \boldsymbol{\nabla}_X \mu$.

Weak form of fine-scale problem

Having established the balance equations and constitutive relations, we can now derive the weak form. The standard space-variational format corresponding to Eqs. (3.14) and (3.16) reads: Find $\boldsymbol{u} \in \mathbb{U}$ and $\mu \in \mathbb{M}$ in the appropriately defined spaces that solve

$$\int_\Omega [\delta\boldsymbol{u} \otimes \boldsymbol{\nabla}_X] : \boldsymbol{P}(\boldsymbol{F}) \, \mathrm{d}\Omega = \int_{\Gamma_\mathrm{N}^{(u)}} \boldsymbol{t}_X^\mathrm{P} \cdot \delta\boldsymbol{u} \, \mathrm{d}\Gamma \quad \forall \delta\boldsymbol{u} \in \mathbb{U}^0, \tag{3.21a}$$

$$-\int_{\Omega_\mathrm{E}} \boldsymbol{\nabla}_X \delta\mu \cdot \boldsymbol{J}(\boldsymbol{F}, \boldsymbol{G}) \, \mathrm{d}\Omega = -\int_{\Gamma_\mathrm{N}^{(\mu)}} \delta\mu \, J^\mathrm{P} \, \mathrm{d}\Gamma \quad \forall \delta\mu \in \mathbb{M}^0, \tag{3.21b}$$

where $\mathbb{U}^0$ and $\mathbb{M}^0$ are the appropriately defined test spaces.

Computational homogenization

Now that the fine-scale problem is defined, we can set up the RVE problem in a multi-scale framework. The first step is to extend the existing RVE volume averaging operator defined in (3.1) to allow for computation of effective properties and effective fluxes via homogenization

$$\langle \bullet \rangle_{\square,\mathrm{E}} := \frac{1}{|\Omega_{\square,\mathrm{E}}|} \int_{\Omega_\square,\mathrm{E}} \bullet \, \mathrm{d}\Omega, \tag{3.22a}$$

$$\phi_0 := \frac{|\Omega_{\square,\mathrm{E}}|}{|\Omega_\square|}. \tag{3.22b}$$

The macro-scale solution must be transmitted to the sub-scale during the prolongation step; this information (loading data) acts as the driving force for the RVE problem. Hence, in the second step, we define the standard prolongation (first order homogenization) rules as follows

$$\boldsymbol{u} = \boldsymbol{u}^\mathrm{M}[\bar{\boldsymbol{u}}] + \boldsymbol{u}^\mathrm{S}, \tag{3.23a}$$

$$\mu = \mu^\mathrm{M}[\bar{\mu}] + \mu^\mathrm{S}, \tag{3.23b}$$

where

$$\boldsymbol{u}^\mathrm{M}[\bar{\boldsymbol{u}}](\bar{\boldsymbol{X}}; \boldsymbol{X}) := \bar{\boldsymbol{u}}(\bar{\boldsymbol{X}}) + \bar{\boldsymbol{H}}[\bar{\boldsymbol{u}}](\bar{\boldsymbol{X}}) \cdot [\boldsymbol{X} - \bar{\boldsymbol{X}}], \quad \bar{\boldsymbol{H}} := \bar{\boldsymbol{u}} \otimes \boldsymbol{\nabla}_X = \bar{\boldsymbol{F}} - \boldsymbol{I}, \tag{3.24a}$$

$$\mu^\mathrm{M}[\bar{\mu}](\bar{\boldsymbol{X}}; \boldsymbol{X}) := \bar{\mu}(\bar{\boldsymbol{X}}) + \bar{\boldsymbol{G}}[\bar{\mu}](\bar{\boldsymbol{X}}) \cdot [\boldsymbol{X} - \bar{\boldsymbol{X}}], \quad \bar{\boldsymbol{G}} := \boldsymbol{\nabla}_X \bar{\mu}. \tag{3.24b}$$

Here, the sub-scale fields $\boldsymbol{u}$ and μ are decomposed into macro-scale parts, $\boldsymbol{u}^{\mathrm{M}}$ and μ^{M}, and micro-scale/fluctuating parts, $\boldsymbol{u}^{\mathrm{S}}$ and μ^{S}.

Using the fine-scale problem (4.9) as a starting point, we can deduce the corresponding macro-scale problem via VCH. The weak form of the macro-scale problem is formulated as follows: Find $\bar{\boldsymbol{u}} \in \bar{\mathbb{U}}$ and $\bar{\mu} \in \bar{\mathbb{U}} \times \bar{\mathbb{M}}$ that solve[2]

$$\int_{\bar{\Omega}} [\delta \bar{\boldsymbol{u}} \otimes \boldsymbol{\nabla}_X] : \bar{\boldsymbol{P}}\{\bar{\boldsymbol{F}}\} \, \mathrm{d}\Omega = \int_{\bar{\Gamma}_{\mathrm{N}}^{(u)}} \bar{\boldsymbol{t}}_X^{\mathrm{P}} \cdot \delta \bar{\boldsymbol{u}} \, \mathrm{d}\Gamma \quad \forall \delta \bar{\boldsymbol{u}} \in \bar{\mathbb{U}}^0, \tag{3.25a}$$

$$-\int_{\bar{\Omega}} \boldsymbol{\nabla}_X \delta \bar{\mu} \cdot \bar{\boldsymbol{J}}\{\bar{\boldsymbol{F}}, \bar{\boldsymbol{G}}\} \, \mathrm{d}\Omega = -\int_{\bar{\Gamma}_{\mathrm{N}}^{(\mu)}} \delta \bar{\mu} \, \bar{J}^{\mathrm{P}} \, \mathrm{d}\Gamma \quad \forall \delta \bar{\mu} \in \bar{\mathbb{M}}^0. \tag{3.25b}$$

The homogenized constitutive quantities are defined as

$$\bar{\boldsymbol{P}} = \langle \boldsymbol{P} \rangle_\square \,, \tag{3.26a}$$

$$\bar{\boldsymbol{J}} = \phi_0 \, \langle \boldsymbol{J} \rangle_{\square, \mathrm{E}} \,, \tag{3.26b}$$

and become implicit functions of $\bar{\boldsymbol{F}}$ and $\bar{\boldsymbol{G}}$ through the RVE problem.

RVE problem

The approach for this RVE problem is to solve the equilibrium and diffusion equations sequentially, as they are only one-way coupled. First, we solve for $\boldsymbol{u}\{\bar{\boldsymbol{F}}\}$ from the equilibrium equation to obtain $\boldsymbol{F} = \boldsymbol{F}\{\bar{\boldsymbol{F}}\} = \boldsymbol{I} + \boldsymbol{u}\{\bar{\boldsymbol{F}}\} \otimes \boldsymbol{\nabla}_X$. In the second step, we use the local deformation gradient $\boldsymbol{F} = \boldsymbol{F}\{\bar{\boldsymbol{F}}\}$ in the RVE to solve for $\mu = \mu\{\bar{\boldsymbol{F}}, \bar{\boldsymbol{G}}\}$ from the diffusion equation.

The weak form of the RVE problem is formulated as follows:

(i) **Equilibrium equation for RVE**
For given $\bar{\boldsymbol{F}}$, find $\boldsymbol{u}\{\bar{\boldsymbol{F}}\} = \boldsymbol{u} \in \mathbb{U}_\square$ and $\boldsymbol{\lambda}(\bar{\boldsymbol{F}}) = \boldsymbol{\lambda} \in \mathbb{L}_\square^u$ that solve

$$\frac{1}{|\Omega_\square|} \int_{\Omega_\square} \boldsymbol{P}(\boldsymbol{I} + \boldsymbol{u} \otimes \boldsymbol{\nabla}_X) : [\delta \boldsymbol{u} \otimes \boldsymbol{\nabla}_X] \, \mathrm{d}\Omega - \frac{1}{|\Omega_\square|} \int_{\Gamma_\square^+} \boldsymbol{\lambda} \cdot [\![\delta \boldsymbol{u}]\!] \, \mathrm{d}\Gamma = 0$$
$$\forall \delta \boldsymbol{u} \in \mathbb{U}_\square, \tag{3.27a}$$

$$-\frac{1}{|\Omega_\square|} \int_{\Gamma_\square^+} \delta \boldsymbol{\lambda} \cdot [\![\boldsymbol{u}]\!] \, \mathrm{d}\Gamma = -\frac{1}{|\Omega_\square|} \int_{\Gamma_\square^+} \delta \boldsymbol{\lambda} \otimes [\![\boldsymbol{X}]\!] \, \mathrm{d}\Gamma : [\bar{\boldsymbol{F}} - \boldsymbol{I}]$$
$$\forall \delta \boldsymbol{\lambda} \in \mathbb{L}_\square^u. \tag{3.27b}$$

---

[2]Here, the $\{\bullet\}$ notation is introduced to denote an implicit dependence.

(ii) **Diffusion equation for RVE**

For given $(\bar{\boldsymbol{F}}, \bar{\boldsymbol{G}})$ and local deformation gradient $\boldsymbol{F}\{\bar{\boldsymbol{F}}\}$, find $\mu\{\bar{\boldsymbol{F}}, \bar{\boldsymbol{G}}\} = \mu \in \mathbb{M}_\square$ and $(\lambda, \hat{\lambda}) \in \mathbb{L}_\square^\mu \times \mathbb{R}$ that solve

$$-\frac{1}{|\Omega_\square|} \int_{\Omega_{\square,\mathrm{E}}} [\boldsymbol{\nabla}_X \delta\mu] \cdot \boldsymbol{J}(\boldsymbol{F}\{\bar{\boldsymbol{F}}\}, \boldsymbol{G}) \, \mathrm{d}\Omega$$

$$+\frac{1}{|\Omega_\square|} \int_{\Gamma_{\square,\mathrm{E}}^+} \lambda \, [\![\delta\mu]\!] \, \mathrm{d}\Gamma - \frac{1}{|\Omega_\square|} \int_{\Omega_{\square,\mathrm{E}}} \delta\mu \, \mathrm{d}\Omega \, \hat{\lambda} = 0$$

$$\forall \delta\mu \in \mathbb{M}_\square, \qquad (3.28\mathrm{a})$$

$$\frac{1}{|\Omega_\square|} \int_{\Gamma_{\square,\mathrm{E}}^+} \delta\lambda \cdot [\![\mu]\!] \, \mathrm{d}\Gamma = \frac{1}{|\Omega_\square|} \int_{\Gamma_{\square,\mathrm{E}}^+} \delta\lambda \, [\![\boldsymbol{X}]\!] \, \mathrm{d}\Gamma \cdot \bar{\boldsymbol{G}}$$

$$\forall \delta\lambda \in \mathbb{L}_\square^\mu, \qquad (3.28\mathrm{b})$$

$$-\frac{1}{|\Omega_\square|} \int_{\Omega_{\square,\mathrm{E}}} \mu \, \mathrm{d}\Omega \, \delta\hat{\lambda} = 0$$

$$\forall \delta\hat{\lambda} \in \mathbb{R}. \qquad (3.28\mathrm{c})$$

The difference operator $[\![\bullet]\!]_\square(\boldsymbol{x}) := \bullet(\boldsymbol{x}) - \bullet(\boldsymbol{x}^-(\boldsymbol{x}))$ is introduced when enforcing weakly periodic boundary conditions (WPBC), cf. [51]. In this context, $\boldsymbol{x} \in \Gamma_\square^+$ represents an image point, while $\boldsymbol{x}^-(\boldsymbol{x}) \in \Gamma^- = \Gamma_\square \setminus \Gamma_\square^+$ is the corresponding mirror point.

For a fixed $\bar{\boldsymbol{F}}$, we see that the linearity of the diffusion problem allows for the decomposition

$$\mu\{\bar{\boldsymbol{F}}, \bar{\boldsymbol{G}}\} = \sum_{i=1}^3 \hat{\mu}_i\{\bar{\boldsymbol{F}}\} \, \bar{G}_i, \qquad (3.29)$$

in terms of sensitivity fields $\hat{\mu}_i\{\bar{\boldsymbol{F}}\}$ for each Cartesian component $G_i := \boldsymbol{G} \cdot \boldsymbol{E}_i$.

For pre-computed local deformation $\boldsymbol{F}\{\bar{\boldsymbol{F}}\}$, the sensitivity field $\hat{\mu}_i\{\bar{\boldsymbol{F}}\} = \hat{\mu}_i \in \mathbb{M}_\square$ together with auxiliary Lagrange multipliers $(\lambda, \hat{\lambda}) \in \mathbb{L}_\square^\mu \times \mathbb{R}$ solve

$$-\frac{1}{|\Omega_\square|} \int_{\Omega_{\square,\mathrm{E}}} [\boldsymbol{\nabla}_X \delta\hat{\mu}] \cdot \boldsymbol{M}(\boldsymbol{F}\{\bar{\boldsymbol{F}}\}) \cdot [\boldsymbol{\nabla}_X \hat{\mu}_i] \, \mathrm{d}\Omega$$

$$+\frac{1}{|\Omega_\square|} \int_{\Gamma_{\square,\mathrm{E}}^+} \lambda [\![\delta\hat{\mu}]\!] \, \mathrm{d}\Gamma - \frac{1}{|\Omega_\square|} \int_{\Omega_{\square,\mathrm{E}}} \delta\hat{\mu}_i \, \mathrm{d}\Omega \, \hat{\lambda} = 0$$

$$\forall \delta\hat{\mu} \in \mathbb{M}_\square, \qquad (3.30\mathrm{a})$$

$$\frac{1}{|\Omega_\square|} \int_{\Gamma_{\square,\mathrm{E}}^+} \delta\lambda \cdot [\![\hat{\mu}_i]\!] \, \mathrm{d}\Gamma = \frac{1}{|\Omega_\square|} \int_{\Gamma_{\square,\mathrm{E}}^+} \delta\lambda \, [\![\boldsymbol{X}]\!] \, \mathrm{d}\Gamma \cdot \boldsymbol{E}_i$$

$$\forall \delta\lambda \in \mathbb{L}_\square^\mu, \qquad (3.30\mathrm{b})$$

$$-\frac{1}{|\Omega_\square|} \int_{\Omega_{\square,\mathrm{E}}} \hat{\mu}_i \, \mathrm{d}\Omega \, \delta\hat{\lambda} = 0$$

$$\forall \delta\hat{\lambda} \in \mathbb{R}. \qquad (3.30\mathrm{c})$$

Consequently, this gives the local flux $\boldsymbol{J}\{\bar{\boldsymbol{F}}, \bar{\boldsymbol{G}}\} = \sum_{i=1}^{3} -\boldsymbol{M}(\boldsymbol{F}\{\bar{\boldsymbol{F}}\}) \cdot [\boldsymbol{\nabla}_X \hat{\mu}_i] \, \bar{G}_i$, resulting in the homogenized flux

$$\bar{\boldsymbol{J}}\{\bar{\boldsymbol{F}}, \bar{\boldsymbol{G}}\} = -\bar{\boldsymbol{M}}\{\bar{\boldsymbol{F}}\} \cdot \bar{\boldsymbol{G}}, \tag{3.31}$$

with

$$\bar{\boldsymbol{M}}\{\bar{\boldsymbol{F}}\} = \sum_{i=1}^{3} \left[\frac{1}{|\Omega_\square|} \int_{\Omega_\square} \boldsymbol{M}(\boldsymbol{F}\{\bar{\boldsymbol{F}}\}) \cdot [\boldsymbol{\nabla}_X \hat{\mu}_i] \, \mathrm{d}\Omega \right] \otimes \boldsymbol{E}_i, \tag{3.32}$$

being the explicit expression for the effective deformation-dependent mobility. As a direct consequence of (3.31), we note that the macro-scale problem of finding $\bar{\mu}$ for a pre-computed solution $\bar{\boldsymbol{u}}$ will, in fact, be linear.

For a coupled boundary value problem, it is natural to consider the Lagrangian form of the transport problem in (3.25b). However, we may also consider the (strong form) macro-scale diffusion equation in the deformed configuration

$$-\bar{\boldsymbol{j}} \cdot \boldsymbol{\nabla} = 0 \text{ in } \bar{\omega}. \tag{3.33}$$

For this problem, we consider $\bar{\mu} = \bar{\mu}(\boldsymbol{x})$, and the effective flux $\boldsymbol{j}$ is given as

$$\bar{\boldsymbol{j}} = -\bar{\boldsymbol{m}}\{\bar{\boldsymbol{F}}\} \cdot \bar{\boldsymbol{g}}, \tag{3.34a}$$

$$\bar{\boldsymbol{m}}\{\bar{\boldsymbol{F}}\} = \frac{1}{\bar{J}} \bar{\boldsymbol{F}} \cdot \bar{\boldsymbol{M}}\{\bar{\boldsymbol{F}}\} \cdot \bar{\boldsymbol{F}}^T, \tag{3.34b}$$

where $\bar{\boldsymbol{m}}\{\bar{\boldsymbol{F}}\}$ is the effective deformation-dependent mobility in the deformed configuration, and $\bar{\boldsymbol{g}} = \bar{\boldsymbol{F}}^{-T} \cdot \bar{\boldsymbol{G}} = \boldsymbol{\nabla}\bar{\mu}$.

Ion transport during compression of SBE

We shall now consider mixed control of the mechanical problem, pertinent to a virtual compression test in z-direction with stress free in-plane expansion. To this end, we restate Eq. (3.27) for the special case that we parametrize the load in $\bar{F}_{33}$ while setting $\bar{F}_{12} = \bar{F}_{23} = \bar{F}_{31} = \bar{F}_{13} = \bar{F}_{21} = \bar{F}_{32} = 0$ and $\bar{P}_{11} = \bar{P}_{22} = 0$.

As a first step, we revisit the decomposition in (3.23a) and seek to solve for the (sub-scale) fluctuation $\boldsymbol{u}^{\mathrm{S}}$. The macro-scale part of the displacement field becomes[3]

$$\boldsymbol{u}^{\mathrm{M}} = \hat{\boldsymbol{F}}(\bar{F}_{11}, \bar{F}_{22}, \bar{F}_{33}) \cdot [\boldsymbol{X} - \bar{\boldsymbol{X}}], \tag{3.35}$$

where we introduce the expression $\hat{\boldsymbol{F}}(\bar{F}_{11}, \bar{F}_{22}, \bar{F}_{33}) = \sum_{i=1}^{3} \bar{F}_{ii} \boldsymbol{E}_i \otimes \boldsymbol{E}_i$ for the diagonal deformation gradient. Here, $\bar{F}_{11}$ and $\bar{F}_{22}$ become global unknowns.

---

[3]We note that the solution is invariant to an arbitrary translation $\bar{\boldsymbol{u}}$, which is omitted here.

The RVE problem can now be stated as: Find $(\boldsymbol{u}^{\mathrm{S}}\{\bar{F}_{33}\}, \bar{F}_{11}\{\bar{F}_{33}\}, \bar{F}_{22}\{\bar{F}_{33}\}) = (\boldsymbol{u}^{\mathrm{S}}, \bar{F}_{11}, \bar{F}_{22}) \in \mathbb{U}_0 \times \mathbb{R} \times \mathbb{R}$, and $\lambda \in \mathbb{L}_\square^u$ that solves

$$\frac{1}{|\Omega_\square|} \int_{\Omega_\square} \boldsymbol{P}(\hat{\boldsymbol{F}}(\bar{F}_{11}, \bar{F}_{22}, \bar{F}_{33}) + \boldsymbol{u}^{\mathrm{S}} \otimes \boldsymbol{\nabla}_X) : [\delta\boldsymbol{u}^{\mathrm{S}} \otimes \boldsymbol{\nabla}_X] \, \mathrm{d}\Omega$$

$$-\frac{1}{|\Omega_\square|} \int_{\Gamma_\square^+} \boldsymbol{\lambda} \cdot [\![\delta\boldsymbol{u}^{\mathrm{S}}]\!] \, \mathrm{d}\Gamma = 0$$

$$\forall \delta\boldsymbol{u}^{\mathrm{S}} \in \mathbb{U}_\square, \qquad (3.36\mathrm{a})$$

$$\delta\bar{F}_{11} \frac{1}{|\Omega_\square|} \int_{\Omega_\square} \boldsymbol{P}(\hat{\boldsymbol{F}}(\bar{F}_{11}, \bar{F}_{22}, \bar{F}_{33}) + \boldsymbol{u}^{\mathrm{S}} \otimes \boldsymbol{\nabla}_X) : [\boldsymbol{E}_1 \otimes \boldsymbol{E}_1] \, \mathrm{d}\Omega = 0$$

$$\forall \delta\bar{F}_{11} \in \mathbb{R}, \qquad (3.36\mathrm{b})$$

$$\delta\bar{F}_{22} \frac{1}{|\Omega_\square|} \int_{\Omega_\square} \boldsymbol{P}(\hat{\boldsymbol{F}}(\bar{F}_{11}, \bar{F}_{22}, \bar{F}_{33}) + \boldsymbol{u}^{\mathrm{S}} \otimes \boldsymbol{\nabla}_X) : [\boldsymbol{E}_2 \otimes \boldsymbol{E}_2] \, \mathrm{d}\Omega = 0$$

$$\forall \delta\bar{F}_{22} \in \mathbb{R}, \qquad (3.36\mathrm{c})$$

$$-\frac{1}{|\Omega_\square|} \int_{\Gamma_\square^+} \delta\boldsymbol{\lambda} \cdot [\![\boldsymbol{u}^{\mathrm{S}}]\!] \, \mathrm{d}\Gamma = 0$$

$$\forall \delta\boldsymbol{\lambda} \in \mathbb{L}_\square^u, \qquad (3.36\mathrm{d})$$

As a result, the macroscopic deformation gradient becomes $\bar{\boldsymbol{F}}\{\bar{F}_{33}\} = \hat{\boldsymbol{F}}(\bar{F}_{11}\{\bar{F}_{33}\}, \bar{F}_{22}\{\bar{F}_{33}\}, \bar{F}_{33})$, and the local deformation gradient needed for the subsequent diffusion problem in (3.30) becomes

$$\boldsymbol{F}\{\bar{\boldsymbol{F}}\{\bar{F}_{33}\}\} = \bar{\boldsymbol{F}}\{\bar{F}_{33}\} + \boldsymbol{u}^{\mathrm{S}}\{\bar{F}_{33}\} \otimes \boldsymbol{\nabla}_X. \qquad (3.37)$$

For illustrative purposes, Figure 3.1 is included to show the ionic flux pathways as the liquid pore space is deforming; it exemplifies how this framework addresses the coupled effects of effective ionic transport and microstructure deformations.
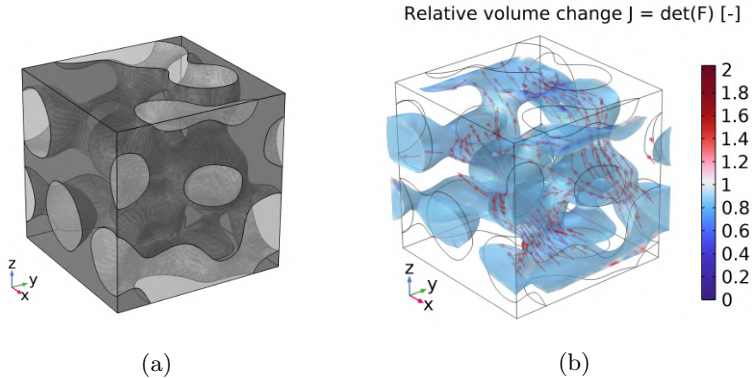
Figure 3.1: *Initial undeformed RVE domain in (a), and corresponding deformed/compressed RVE with ionic flux vectors in (b). The solid polymer is highlighted in dark gray, while the liquid electrolyte is highlighted in light gray.*

3.4   Related collaborative works

In this section, we showcase various collaborative efforts on SBE modeling. The methods outlined in this thesis have led to significant contributions to the computational results of these co-authored papers; in particular, we exploit the same overarching framework of virtual material testing of SBEs based on **Paper A** and **Paper D**.

3D RVE reconstruction based on FIB-SEM data

In our joint research with Duan et al. [52], we employ combined focused ion beam and scanning electron microscopy (FIB-SEM) to obtain high-resolution 3D data of the SBE microstructure. Initially, serial milling with FIB is carried out at the nanometer scale to reveal the underlying microstructure morphology. Subsequently, high-resolution 2D images are captured using SEM. The acquired 2D image sequences are then assembled into a 3D structure. In a post-processing step, the solid and liquid phase are identified, respectively. Finally, voxel-based 3D RVE meshes are generated for the different phases. See Figure 3.2 for an overview of the 3D RVE reconstruction process.

In generating the RVEs from 2D FIB-SEM images, the procedure involves extruding pixels to form voxels. The extrusion depth corresponds to the gap distance between each FIB-SEM image, i.e., 20 nm. The advantage of using a voxel based geometry in this case is that an accurate and well-defined geometry, from experimental data, can easily be prepared for FEM simulation. In fact, each voxel of the geometry is represented by a hexahedron element in the RVE mesh.

For illustrative purposes, Figure 3.3 is included to show the size of the experimentally acquired RVEs. Just like in **Paper A**, c.f. Section 3.1 and 3.2, the goal is to compute effective stiffness and ionic conductivity for the voxel-based 3D RVEs.

It should be noted that the issue with voxel based geometries is that they tend to scale in complexity with respect to the imaging resolution, resulting in computationally
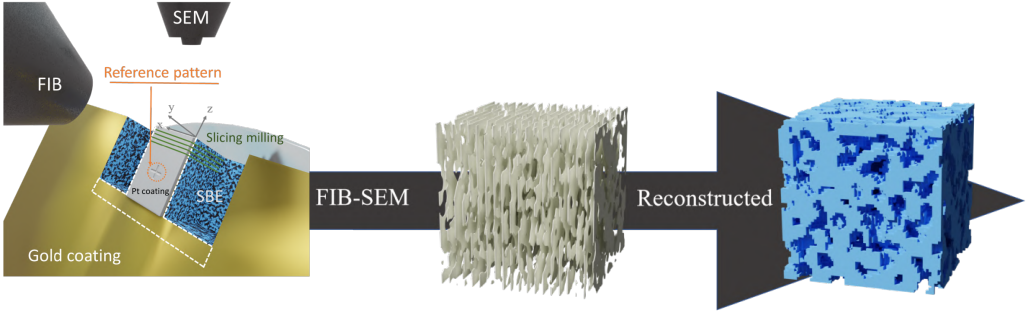
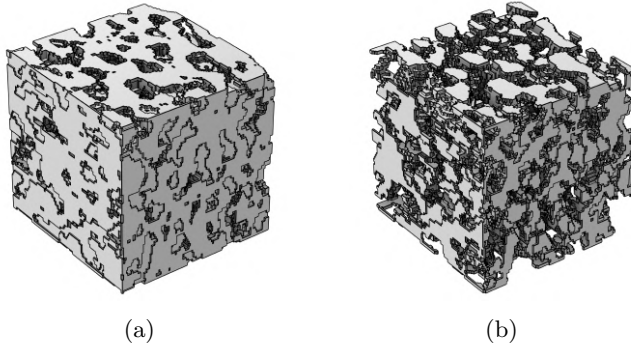Figure 3.2: *Overview of the FIB-SEM process to reconstruct 3D SBE microstructures. From Duan et al. [52].*

| (a) | (b) |

Figure 3.3: *Voxel-based RVE of solid polymer domain in (a) and liquid electrolyte domain in (b). Geometric dimensions of the RVEs are 1.180 x 1.220 x 1.180 μm^3.*

expensive RVEs. In this case, the RVEs are discretized with up to 400k elements with some of the problems solving up to 12 million dofs. The simulations are performed in COMSOL Multiphysics, see Figure 3.4 for the results. Figure 3.4 clearly shows the trade-off between effective stiffness and effective ionic conductivity depending on the ratio between the solid phase and liquid phase. As expected, the effective stiffness increases with increasing volume fraction of solid phase, while the effective ionic conductivity increases with increasing volume fraction of liquid phase. However, the unexpected part about the simulation results in Figure 3.4 is the fact that the volume fraction varies within a range of 10%. This indicates that the volume fraction is not constant throughout the whole SBE sample, and that the simulation results are slightly sensitive to where the RVEs are sampled from on the (large) 2D FIB-SEM images.

Based on experimental data, the solid polymer is assumed to have the intrinsic stiffness 2.167 GPa and intrinsic Poisson's ratio of 0.33, while the neat liquid electrolyte is assumed to have an intrinsic ionic conductivity of 4.35 mS/cm. Upon averaging the RVE data points, we obtain the average effective stiffness $\bar{E} = 738.1725$ MPa with a standard deviation of 85.6112 MPa, and average effective ionic conductivity $\bar{D} = 0.6328$ mS/cm
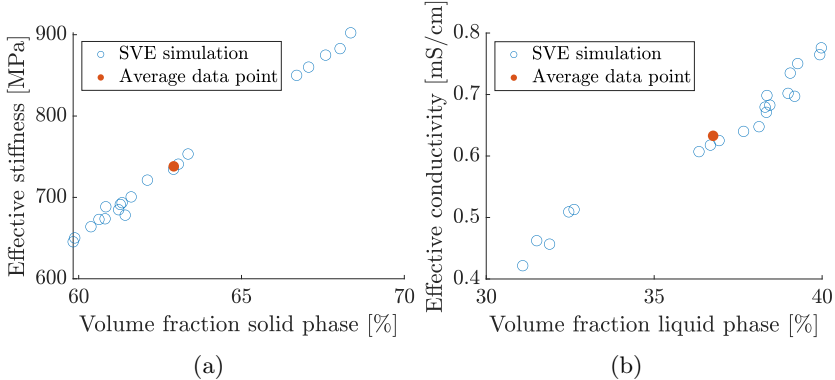
Figure 3.4: *RVE simulations assuming (a) linear elasticity for effective stiffness, (b) linear Fickian diffusion for effective ionic conductivity. Each sample is denoted as a Statistical Volume Element (SVE) since they are sampled from different locations of the (large) 2D FIB-SEM images.*

with standard deviation of 0.1069 mS/cm. It should be noted that the ensemble average is properly performed only if all RVE samples have the same volume fraction, but this is not the case here. Since there is a small spread in the volume fraction, the ensemble average is not the most suitable choice of average metric.

Lastly, it should be mentioned that the simulation results on the average effective stiffness $\bar{\mathsf{E}} = 738.1725$ MPa and average effective ionic conductivity $\bar{D} = 0.6328$ mS/cm act as upper bounds for the effective properties. The reason is because Dirichlet boundary conditions, which produce slightly stiffer simulation results, are enforced on the fluctuation fields. While periodic boundary conditions would be the preferred option, this choice is based on the fact that periodic boundary conditions cannot be used for non-periodic RVE geometries.

Effective permeability based on Stokes flow

In collaboration with Carlstedt et al. [32], we analyze the structural battery assuming poroelasticity for the SBE. In particular, we derive the effective permeability for (macro-scale) Darcy's law by homogenizing the fluid flow velocity solved from (sub-scale) Stokes flow [53]. The governing equations for stationary Stokes flow are

$$-\mu\boldsymbol{\nabla}^2\boldsymbol{v} + \boldsymbol{\nabla}p = \boldsymbol{0} \quad \text{in } \Omega_{\text{E}}, \tag{3.38a}$$

$$\boldsymbol{v} \cdot \boldsymbol{\nabla} = 0 \quad \text{in } \Omega_{\text{E}}, \tag{3.38b}$$

$$\boldsymbol{v} = \boldsymbol{0} \quad \text{on } \Gamma_{\text{S/E}}, \tag{3.38c}$$

where μ is the dynamic viscosity, $\boldsymbol{v}$ is the velocity field and p is the pressure. This problem is solved in COMSOL Multiphysics using quadratic shape functions for the velocity field and linear basis functions for the pressure field, in order to satisfy the LBB condition arising from the saddle-point problem in the variational formulation.
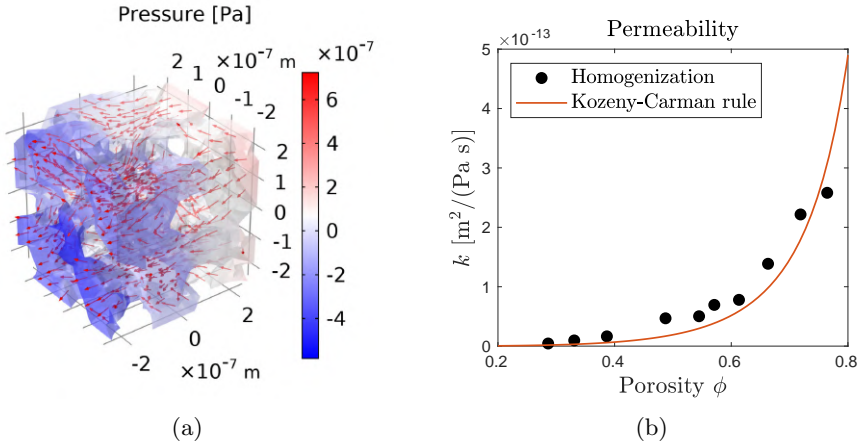
21

Figure 3.5: *The fluid pressure and velocity vectors are shown in (a), while the scalar effective permeability is shown in (b).*

Assuming the linear macro-scale relation for Darcy's law

$$\bar{\boldsymbol{w}} = -\bar{\boldsymbol{K}} \cdot \bar{\boldsymbol{g}}^{(p)}, \tag{3.39}$$

where $\bar{\boldsymbol{w}}$ is the seepage velocity and $\bar{\boldsymbol{g}}^{(p)}$ is the pressure gradient $\boldsymbol{\nabla}p$, we compute the effective permeability as

$$\bar{\boldsymbol{K}} = -\sum_{i=1}^{3} \phi \left\langle \boldsymbol{v}^{(i)} \right\rangle_{\square} \otimes \boldsymbol{e}_i. \tag{3.40}$$

The homogenized permeability from RVEs can be used to calibrate the Kozeny-Carman rule, which predicts the effective isotropic permeability as a function of porosity

$$k = d_{\mathrm{p}}^2 \frac{\phi^3}{180 \, (1-\phi)^2}. \tag{3.41}$$

Here, ϕ is the porosity, and d_{p} (diameter of the volume equivalent spherical particle) corresponds to the only unknown material parameter that is calibrated against the homogenized permeability values from RVE computations. The effective permeability tensor is assumed to be isotropic; hence, scalar quasi-isotropic permeability values are computed according to Section 3.2. See Figure 3.5 for the results.

4 Multi-scale modeling of electro-chemical systems

So far, the effective ionic conductivity of SBEs has been treated in a simplified fashion where the combined electro-chemical potential $\mu_{\mathrm{EC}} := \mu + Fz\varphi$ is assumed to exist only in the liquid electrolyte domain (**Paper A** and **Paper D**). This assumption is reasonable if the electric potential field is trivial, making it sensible to combine both potentials for an electro-chemical potential gradient $\boldsymbol{\nabla}\mu_{\mathrm{EC}}$, which serves as the driving force in a Fickian constitutive model for ionic flux. However, it is important to note that the electric potential φ will in reality also permeate the solid domain. Thus, if the microstructure morphology is highly complex and the porosity is low, the chemical potential field μ will be significantly different from the electric potential field φ.

In **Paper B**, the electric potential field is properly resolved to obtain the true electro-chemical potential. Therefore, we formulate the balance equations for the electro-chemically coupled transient transport of electro-active species in the SBE. Additionally, the relevant constitutive relations in the liquid electrolyte domain Ω_{E} and the solid polymer domain Ω_{S} are defined. Although all equations pertaining to ion transport are valid for any number of ions $\alpha = 1, 2, \ldots, N$, the considered electro-chemical system will in practice consist of Li-ions (Li$^+$) and a corresponding companion anion (e.g. PF$_6^-$) that is simply denoted X$^-$.

4.1 Governing equations

A rigorous treatment of electro-chemically coupled ion transport would require resolving the electric potential field via Maxwell's equations to model ionic migration, but by making the critical assumption that the magnetic field is assumed to vary slowly, the formulation is simplified to electrostatics where the electric field conveniently depends solely on the electric potential gradient. For electro-chemical systems that involve N mass balance equations (one for each species), the number of unknowns becomes $N + 1$ due to N chemical potentials and one electric potential. Therefore, an additional equation is required; the most common choice in the battery modeling community is the assumption of electroneutrality [34].

Balance equations

Assuming once again a biphasic material such as the SBE, and exploiting the assumption of electroneutrality results in the following formulation

$$\sum_{\alpha} z_{\alpha} c_{\alpha} = 0, \quad \text{in } \Omega_{\mathrm{E}} \times (0, T], \tag{4.1a}$$

$$\partial_{\mathrm{t}} c_{\alpha} + \boldsymbol{j}_{\alpha} \cdot \boldsymbol{\nabla} = 0 \quad \text{in } \Omega_{\mathrm{E}} \times (0, T], \tag{4.1b}$$

with suitable boundary conditions, constitutive relations, and initial conditions. Here, the first equation represents the electroneutrality assumption while the second equation

expresses mass conservation for species α. The quantity $\boldsymbol{i}$ is the current density, c_α the molar concentration, and $\boldsymbol{j_\alpha}$ the ion mass flux.

However, since electroneutrality is not a fundamental law, it can lead to paradoxes in certain situations. Dickinson et al. [26] showed that electroneutrality is not automatically consistent with Maxwell's equations; especially the electric field can become erroneous [25]. A more correct formulation is to replace the electroneutrality condition with Gauss' law [54]; this will not only give a better prediction of the electric field, but also be able to resolve the electric potential in the solid phase of a biphasic material.

Hence, restricting to electrostatics, we seek the electric potential $\varphi(\boldsymbol{x}, t)$ and the chemical potentials $\mu_\alpha(\boldsymbol{x}, t)$, $\alpha = 1, 2, \ldots, N$, that solve the system

$$\rho - \boldsymbol{d} \cdot \boldsymbol{\nabla} = 0 \quad \text{in } \Omega \times (0, T], \tag{4.2a}$$

$$\partial_t c_\alpha + \boldsymbol{j}_\alpha \cdot \boldsymbol{\nabla} = 0 \quad \text{in } \Omega_E \times (0, T], \tag{4.2b}$$

with suitable boundary conditions, constitutive relations, and the initial condition

$$c_\alpha(\bullet, 0) = c_{\alpha,0} \quad \text{in } \Omega_E. \tag{4.3}$$

Here, the first equation represents Gauss' law which (unlike electroneutrality) properly resolves the electric field. The quantity ρ is the free charge density (per unit volume) and $\boldsymbol{d}$ is the electric flux density (electric displacement field).

Constitutive relations

The electric flux density $\boldsymbol{d}$ and the ion mass flux $\boldsymbol{j}_\alpha$ are defined as

$$\boldsymbol{d} := \boldsymbol{\epsilon} \cdot \boldsymbol{E}, \quad \boldsymbol{E}[\varphi] := -\boldsymbol{\nabla}\varphi, \tag{4.4a}$$

$$\boldsymbol{j}_\alpha := -\boldsymbol{M}_\alpha \cdot [\boldsymbol{\nabla}\mu_\alpha + z'_\alpha \boldsymbol{\nabla}\varphi], \tag{4.4b}$$

where φ is the electric potential and μ_α the chemical potential of a mobile species ($\alpha = 1, 2, \ldots, N$) with the ionic charge $z'_\alpha = F z_\alpha$. Here, F corresponds to the Faraday constant and z_α is the valancy of species α. The material properties are given as the electric permittivity $\boldsymbol{\epsilon}$ and the ionic mobility $\boldsymbol{M}_\alpha$ of species α. In the simple case of material isotropy, they can be condensed to the scalar electric permittivity ϵ and the scalar ionic mobility M_α.

Additionally, the free charge density ρ and the molar concentration c_α are defined as

$$\rho := \begin{cases} \sum_{\alpha=1}^{N} z'_\alpha c_\alpha & \text{in } \Omega_E, \\ 0 & \text{in } \Omega_S, \end{cases} \tag{4.5a}$$

$$c_\alpha := c_\alpha(\mu_\alpha) \quad \text{in } \Omega_E. \tag{4.5b}$$

In the simplest approach, we assume a dilute distribution of charged ions in the electrolyte. Thus, the concentration c_α is related to the chemical potential μ_α as follows

$$\mu_\alpha = \mu_{\alpha,0} + RT \ln(\gamma_\alpha c_\alpha), \tag{4.6}$$

where $\mu_{\alpha,0}$ is the reference chemical potential of species α, R the gas constant, T the temperature and γ_α the activity coefficient of species α. If the concentration is assumed to have small fluctuations around the concentration level $c_\alpha = c_{\alpha,0}$, then the relation (4.6) can be linearized. Linearization of (4.6) around $c_\alpha = c_{\alpha,0}$ with the assumption $\mu_{\alpha,0} = -RT \ln(\gamma_\alpha c_{\alpha,0})$ results in the relation

$$c_\alpha = k_\alpha \mu_\alpha + c_{\alpha,0}, \tag{4.7}$$

where k_α depends on the choice of γ_α. Choosing γ_α such that it is constant results in the simple relation $k_\alpha = \frac{c_{\alpha,0}}{RT}$.

Finally, the current density in the electro-chemical system can be computed via Faraday's rule of electrolysis as a post-processing quantity as

$$\boldsymbol{i} := \sum_{\alpha=1}^{N} z'_\alpha \boldsymbol{j}_\alpha. \tag{4.8a}$$

Weak formulation of fine-scale problem

With the governing equations established, the corresponding weak formulation at every time instance reads: find $(\varphi, \mu_\alpha) \in \mathbb{P} \times \mathbb{M}_\alpha$ that solve

$$\int_\Omega \delta\varphi\, \rho \,\mathrm{d}\Omega + \int_\Omega \boldsymbol{\nabla}\delta\varphi \cdot \boldsymbol{d} \,\mathrm{d}\Omega = \int_{\Gamma_{\mathrm{N}}^{(\varphi)}} \delta\varphi\, d^{\mathrm{p}} \,\mathrm{d}\Gamma$$
$$\forall \delta\varphi \in \mathbb{P}^0, \tag{4.9a}$$

$$\int_{\Omega_{\mathrm{E}}} \delta\mu_\alpha\, \partial_{\mathrm{t}} c_\alpha \,\mathrm{d}\Omega - \int_{\Omega_{\mathrm{E}}} \boldsymbol{\nabla}\delta\mu_\alpha \cdot \boldsymbol{j}_\alpha \,\mathrm{d}\Omega = - \int_{\Gamma_{\mathrm{N}}^{(\alpha)}} \delta\mu_\alpha\, j_\alpha^{\mathrm{p}} \,\mathrm{d}\Gamma$$
$$\forall \delta\mu_\alpha \in \mathbb{M}_\alpha^0, \tag{4.9b}$$

for $\alpha = 1, 2, \ldots, N$ and appropriately defined initial conditions. Here, Neumann boundary conditions $\boldsymbol{d} \cdot \boldsymbol{n} := d^{\mathrm{p}}$ and $\boldsymbol{j}_\alpha \cdot \boldsymbol{n} := j_\alpha^{\mathrm{p}}$ are prescribed on $\Gamma_N^{(\varphi)}$ and $\Gamma_N^{(\alpha)}$ respectively. Exact definitions of the trial and test spaces are left out for brevity.

4.2 Variationally consistent homogenization

So far, only the fine-scale (single-scale) problem has been established. However, performing Direct Numerical Simulations (DNS) to account for microstructure features (e.g. SBE pores) that are several orders of magnitude smaller than the component level (e.g. battery scale) is computationally infeasible. As a consequence, numerous multi-scale methods that provide more efficient solution strategies have been developed; see Multiscale Finite Element Method (MsFEM) [55], Heterogeneous Multiscale Methods (HMM) [56], and Variational MultiScale (VMS) [57] to name a few.

Here, the concept of Variationally Consistent Homogenization (VCH) [58] is adopted. As a result, a smooth macro-scale problem and a sub-scale RVE problem can be deduced solely from the fine-scale problem. The steps required in order to achieve this are as follows:

(i) Introduce the running average approximation

$$\int_\Omega \bullet \, \mathrm{d}\Omega \approx \int_\Omega \langle \bullet \rangle_\square (\bar{\boldsymbol{x}}) \, \mathrm{d}\Omega \quad \bar{\boldsymbol{x}} \in \Omega, \tag{4.10}$$

where all fine-scale quantities ($\forall \, \bar{\boldsymbol{x}} \in \Omega$) are approximated as the volume average (over $\Omega_\square$) in the RVE. Here, the RVE domain is assumed to be centered at $\bar{\boldsymbol{x}}$.

(ii) Assume scale separation via first order homogenization

$$\varphi(\bar{\boldsymbol{x}}; \boldsymbol{x}, t) = \bar{\varphi}(\bar{\boldsymbol{x}}, t) + \boldsymbol{\nabla}\bar{\varphi}(\bar{\boldsymbol{x}}, t) \cdot [\boldsymbol{x} - \bar{\boldsymbol{x}}] + \varphi^{\mathrm{S}}(\bar{\boldsymbol{x}}; \boldsymbol{x}, t) \tag{4.11a}$$

$$\mu_\alpha(\bar{\boldsymbol{x}}; \boldsymbol{x}, t) = \bar{\mu}_\alpha(\bar{\boldsymbol{x}}, t) + \boldsymbol{\nabla}\bar{\mu}_\alpha(\bar{\boldsymbol{x}}, t) \cdot [\boldsymbol{x} - \bar{\boldsymbol{x}}] + \mu_\alpha^{\mathrm{S}}(\bar{\boldsymbol{x}}; \boldsymbol{x}, t) \tag{4.11b}$$

where the decomposition corresponds to a first order Taylor expansion $\bar{\bullet}(\bar{\boldsymbol{x}}, t) + \boldsymbol{\nabla}\bar{\bullet}(\bar{\boldsymbol{x}}, t) \cdot [\boldsymbol{x} - \bar{\boldsymbol{x}}]$ around $\bar{\boldsymbol{x}}$ and a fluctuation field $\bullet^{\mathrm{S}}(\bar{\boldsymbol{x}}; \boldsymbol{x}, t)$. Henceforth, the notation on the explicit choice of RVE at macro-scale position $\bar{\boldsymbol{x}}$ is left out for brevity. Moreover, the gradients are shortened as $\bar{\boldsymbol{g}}^\varphi := \boldsymbol{\nabla}\bar{\varphi}$ and $\bar{\boldsymbol{g}}_\alpha^\mu := \boldsymbol{\nabla}\bar{\mu}_\alpha$.

Macro-scale problem

The macro-scale problem is obtained upon testing with only the macroscopic test functions. Hence, the weak formulation at every time instance reads: find $(\bar{\varphi}, \bar{\mu}_\alpha) \in \bar{\mathbb{P}} \times \bar{\mathbb{M}}_\alpha$ that solve

$$\int_\Omega \delta\bar{\varphi} \, \bar{\rho} + \boldsymbol{\nabla}\delta\bar{\varphi} \cdot \bar{\boldsymbol{\rho}}^{(2)} + \boldsymbol{\nabla}\delta\bar{\varphi} \cdot \bar{\boldsymbol{d}} \, \mathrm{d}\Omega = - \int_{\Gamma_{\mathrm{N}}^{(\varphi)}} \delta\bar{\varphi} \, \bar{d}^{\mathrm{p}} \, \mathrm{d}\Gamma$$
$$\forall \delta\bar{\varphi} \in \bar{\mathbb{P}}^0, \tag{4.12a}$$

$$\int_\Omega \delta\bar{\mu}_\alpha \, \partial_{\mathrm{t}}\bar{c}_\alpha + \boldsymbol{\nabla}\delta\bar{\mu}_\alpha \cdot \partial_{\mathrm{t}}\bar{\boldsymbol{c}}_\alpha^{(2)} - \boldsymbol{\nabla}\delta\bar{\mu}_\alpha \cdot \bar{\boldsymbol{j}}_\alpha \, \mathrm{d}\Omega = - \int_{\bar{\Gamma}_{\mathrm{N},\alpha}^{(\mu)}} \delta\bar{\mu}_\alpha \, \bar{j}_\alpha^{\mathrm{p}} \, \mathrm{d}\Gamma$$
$$\forall \delta\bar{\mu}_\alpha \in \bar{\mathbb{M}}_\alpha^0, \tag{4.12b}$$

for $\alpha = 1, 2, \dots, N$ and appropriately defined initial conditions. As a result of VCH, we obtain $\bar{\boldsymbol{\rho}}^{(2)}$ and $\bar{\boldsymbol{c}}_\alpha^{(2)}$ that represent higher order non-standard conservation terms, while the rest are classical averages. Exact definitions of the trial and test spaces are left out for brevity.

Sub-scale RVE problem

The sub-scale RVE problem can be obtained upon testing with only the microscopic test functions. However, since the macroscopic parts of the solutions are treated as known loading data to the sub-scale RVE problem, we may instead seek the full solution as follows: for the given loading histories $\bar{\varphi}(t)$, $\bar{\boldsymbol{g}}^\varphi(t)$, $\bar{\mu}_\alpha(t)$, $\bar{\boldsymbol{g}}_\alpha^\mu(t)$ at every time instance;

find $\varphi \in \mathbb{P}_\square$, $\mu_\alpha \in \mathbb{M}_{\square,\alpha}$, $\lambda^{(\varphi)} \in \mathbb{T}_\square^{(\varphi)}$, $\lambda_\alpha^{(\mu)} \in \mathbb{T}_\square^{(\mu)}$, $\hat{\lambda}^{(\varphi)} \in \mathbb{R}$, $\hat{\lambda}_\alpha^{(\mu)} \in \mathbb{R}$ that solve

$$\langle \delta\varphi\, \rho \rangle_\square + \langle \boldsymbol{\nabla}\delta\varphi \cdot \boldsymbol{d} \rangle_\square - \frac{1}{|\Omega_\square|} \int_{\Gamma_\square^+} [\![\delta\varphi]\!]_\square\, \lambda^{(\varphi)}\, \mathrm{d}\Gamma - \langle \delta\varphi \rangle_\square\, \hat{\lambda}^{(\varphi)} = 0$$

$$\forall \delta\varphi \in \mathbb{P}_\square, \tag{4.13a}$$

$$-\frac{1}{|\Omega_\square|} \int_{\Gamma_\square^+} [\![\varphi]\!]_\square\, \delta\lambda^{(\varphi)}\, \mathrm{d}\Gamma = -\frac{1}{|\Omega_\square|} \int_{\Gamma_\square^+} [\![\boldsymbol{x}]\!]_\square\, \delta\lambda^{(\varphi)}\, \mathrm{d}\Gamma \cdot \bar{\boldsymbol{g}}^\varphi$$

$$\forall \delta\lambda^{(\varphi)} \in \mathbb{T}_\square^{(\varphi)}, \tag{4.13b}$$

$$-\langle \varphi \rangle_\square\, \delta\hat{\lambda}^{(\varphi)} = -\bar{\varphi}\, \delta\hat{\lambda}^{(\varphi)}$$

$$\forall \delta\hat{\lambda}^{(\varphi)} \in \mathbb{R}, \tag{4.13c}$$

$$\phi\, \langle \delta\mu_\alpha\, \partial_t c_\alpha \rangle_{\square,\mathrm{E}} - \phi\, \langle \boldsymbol{\nabla}\delta\mu_\alpha \cdot \boldsymbol{j}_\alpha \rangle_{\square,\mathrm{E}}$$

$$+\frac{1}{|\Omega_\square|} \int_{\Gamma_{\square,\mathrm{E}}^+} [\![\delta\mu_\alpha]\!]_\square\, \lambda_\alpha^{(\mu)}\, \mathrm{d}\Gamma - \phi\langle \delta\mu_\alpha \rangle_{\square,\mathrm{E}}\, \hat{\lambda}_\alpha^{(\mu)} = 0$$

$$\forall \delta\mu_\alpha \in \mathbb{M}_{\square,\alpha}, \tag{4.13d}$$

$$\frac{1}{|\Omega_\square|} \int_{\Gamma_{\square,\mathrm{E}}^+} [\![\mu_\alpha]\!]_\square\, \delta\lambda_\alpha^{(\mu)}\, \mathrm{d}\Gamma = \frac{1}{|\Omega_\square|} \int_{\Gamma_{\square,\mathrm{E}}^+} [\![\boldsymbol{x}]\!]_\square\, \delta\lambda_\alpha^{(\mu)}\, \mathrm{d}\Gamma \cdot \bar{\boldsymbol{g}}_\alpha^\mu$$

$$\forall \delta\lambda_\alpha^{(\mu)} \in \mathbb{T}_\square^{(\mu)}, \tag{4.13e}$$

$$-\phi\langle \mu_\alpha \rangle_{\square,\mathrm{E}}\, \delta\hat{\lambda}_\alpha^{(\mu)} = -\phi(\bar{\mu}_\alpha + \bar{\boldsymbol{g}}_\alpha^\mu \cdot [\bar{\boldsymbol{x}}_\mathrm{E} - \bar{\boldsymbol{x}}])\, \delta\hat{\lambda}_\alpha^{(\mu)}$$

$$\forall \delta\hat{\lambda}_\alpha^{(\mu)} \in \mathbb{R}, \tag{4.13f}$$

for $\alpha = 1, 2, \ldots, N$ and appropriately defined initial conditions. Upon enforcing weakly periodic boundary conditions (WPBC) [51], we use the difference operator $[\![\bullet]\!]_\square(\boldsymbol{x}) := \bullet(\boldsymbol{x}) - \bullet(\boldsymbol{x}^-(\boldsymbol{x}))$. Here, $\boldsymbol{x} \in \Gamma_\square^+$ is an image point whereas $\boldsymbol{x}^-(\boldsymbol{x}) \in \Gamma^- = \Gamma_\square \setminus \Gamma_\square^+$ is the corresponding "mirror point". Additionally, while $\langle \bullet \rangle_\square$ is the RVE volume average operator over the full RVE domain, the operator $\langle \bullet \rangle_{\square,\mathrm{E}}$ is restricted to the liquid phase of the SBE. Note that (4.13a) and (4.13d) correspond to Gauss' law and ion mass conservation, respectively. The rest are constraint equations; (4.13b) and (4.13e) represent WPBCs, while (4.13c) and (4.13f) represent RVE volume average constraints pertaining to proper scale-bridging. Details on the RVE constraints, and exact definitions of the trial and test spaces are left out for brevity.

Solving two-scale models

Two-scale models are often solved via the Finite Element squared (FE^2) method. In this procedure, the macro-scale and the sub-scale RVE problem are solved in a nested fashion with information passing between the scales in both directions. The macro-scale solution is sent to the sub-scale RVE (prolongation), and serves as the driving force ("loading data") to the problem. After solving the sub-scale RVE problem, effective properties (effective fluxes in VCH) are computed and sent back to the macro-scale (homogenization).

In practice, numerical integration is carried out only at quadrature points; hence, only one sub-scale RVE computation per macroscopic quadrature point is needed. However,

for complex 3D macro-scale domains, the number of quadrature points rapidly increases; thus, requiring a large number of sub-scale RVE computations. Together with the fact that the sub-scale RVE itself might also be complex, the FE^2 procedure quickly becomes computationally infeasible.

For certain problems, a viable approach is to exploit the assumption of micro-stationarity to enable a priori upscaling. In such a case, the two-scale model is condensed to a macro-scale problem with precomputed expressions for effective quantities. This circumvents the need for performing RVE computations at every macroscopic quadrature point for all time steps; instead, the homogenization of the (stationary) RVE is performed once and for all.

4.3   Two-scale model with a priori upscaling

Upon introducing the assumption of micro-stationarity, we may pre-compute expressions for effective fluxes. This allows us to solve a macro-scale problem that accounts for the underlying sub-scale RVE through a priori upscaling. Consider the following split of the sub-scale RVE solution fields

$$\varphi(\boldsymbol{x}, t) = \varphi^{\text{stat}}(\boldsymbol{x}, t) + \varphi^{\text{trans}}(\boldsymbol{x}, t), \tag{4.14a}$$

$$\mu_\alpha(\boldsymbol{x}, t) = \mu_\alpha^{\text{stat}}(\boldsymbol{x}, t) + \mu_\alpha^{\text{trans}}(\boldsymbol{x}, t), \tag{4.14b}$$

where the (unconventional) notation "stationary" refers to the steady-state response due to sustained loading, while "transient" refers to the response that contains relaxation processes when the loading is applied quickly as compared to the relaxation time.

The stationary solutions can be obtained upon removing all time derivatives from (4.13); the exact formulation of the stationary problem is left out for brevity. However, the stationary solutions can also be computed as a linear combination of sensitivity fields with time-dependent coefficients corresponding to macroscopic load histories. The decomposition of the stationary solutions is performed as follows

$$\varphi^{\text{stat}}(\boldsymbol{x}, t) = \varphi_{\bar{\varphi}}(\boldsymbol{x})\, \bar{\varphi}(t) + \boldsymbol{\varphi}_{\bar{g}^\varphi}(\boldsymbol{x}) \cdot \bar{\boldsymbol{g}}^\varphi(t)$$
$$+ \sum_{\alpha=1}^{N} \left(\varphi_{\bar{\mu}_\alpha}(\boldsymbol{x})\bar{\mu}_\alpha(t) + \boldsymbol{\varphi}_{\bar{g}_\alpha^\mu}(\boldsymbol{x}) \cdot \bar{\boldsymbol{g}}_\alpha^\mu(t) \right), \tag{4.15a}$$

$$\mu_\alpha^{\text{stat}}(\boldsymbol{x}, t) = \mu_{\alpha, \bar{\varphi}}(\boldsymbol{x})\, \bar{\varphi}(t) + \boldsymbol{\mu}_{\alpha, \bar{g}^\varphi}(\boldsymbol{x}) \cdot \bar{\boldsymbol{g}}^\varphi(t)$$
$$+ \sum_{\beta=1}^{N} \left(\mu_{\alpha, \bar{\mu}_\beta}(\boldsymbol{x})\bar{\mu}_\beta(t) + \boldsymbol{\mu}_{\alpha, \bar{g}_\beta^\mu}(\boldsymbol{x}) \cdot \bar{\boldsymbol{g}}_\beta^\mu(t) \right), \tag{4.15b}$$

where each sensitivity field $\left[\varphi_{\bar{\varphi}}, \boldsymbol{\varphi}_{\bar{g}^\varphi}, \varphi_{\bar{\mu}_\alpha}, \boldsymbol{\varphi}_{\bar{g}_\alpha^\mu}, \mu_{\alpha, \bar{\varphi}}, \boldsymbol{\mu}_{\alpha, \bar{g}^\varphi}, \mu_{\alpha, \bar{\mu}_\beta}, \boldsymbol{\mu}_{\alpha, \bar{g}_\beta^\mu} \right]$ is given by each corresponding time-independent unit sensitivity problem; the exact formulations of the unit sensitivity problems are left out for brevity, see **Paper B**. Based on (4.15), the effective constitutive quantities can be explicitly defined as function of macro-scale data.

For illustration, the effective current density under assumption of micro-stationarity is defined as

$$\bar{\boldsymbol{d}}^{\text{stat}}(\boldsymbol{x}, t) = -\langle \boldsymbol{\epsilon} \cdot (\boldsymbol{\nabla} \otimes \boldsymbol{\varphi}_{\bar{g}^\varphi}) \rangle_\square \cdot \bar{\boldsymbol{g}}^\varphi(t) - \sum_{\alpha=1}^{N} \langle \boldsymbol{\epsilon} \cdot \boldsymbol{\nabla} \rho_{\bar{\mu}_\alpha} \rangle_\square \, \bar{\mu}_\alpha(t)$$

$$- \sum_{\alpha=1}^{N} \langle \boldsymbol{\epsilon} \cdot (\boldsymbol{\nabla} \otimes \boldsymbol{\varphi}_{\bar{g}_\alpha^\mu}) \rangle_\square \cdot \bar{\boldsymbol{g}}_\alpha^\mu(t), \tag{4.16}$$

where $\bar{\boldsymbol{g}}^\varphi(t)$, $\bar{\mu}_\alpha(t)$ and $\bar{\boldsymbol{g}}_\alpha^\mu(t)$ correspond to known loading data that stem from the macro-scale solution. Therefore, the effective quantities simply scale linearly with the "input signals" from the macro-scale problem. Remaining effective fluxes, based on micro-stationarity, are left out for brevity.

With all of this, the homogenization of the (stationary) RVE can now be performed once and for all; resulting in an efficient solution scheme of the, otherwise expensive, two-scale model. This strategy is pursued in **Paper B**.

5 Numerical Model Reduction

Until now, we have not been able to perform fully transient two-scale simulations. The approach taken in **Paper B** relies on the micro-transients to be small. When large micro-transients occur, the micro-stationarity assumption leads to a poor approximation.

To overcome the limitations of the micro-stationarity assumption, **Paper C** focuses on the development of a Numerical Model Reduction (NMR) framework for multi-scale modeling of electro-chemically coupled ion transport, where micro-transients are accounted for. Upon introducing the governing equations and employing Variationally Consistent Homogenization (VCH), a two-scale model consisting of a macro-scale and a sub-scale problem is obtained. Instead of solving for the computationally expensive[1] FE^2 problem where the macro-scale and sub-scale problems are solved in a nested fashion, we exploit NMR for the RVE problem by training a surrogate model that replaces the sub-scale finite element simulations. The surrogate model is trained by performing Proper Orthogonal Decomposition (POD) on snapshots of the primary fields. Each macro-scale quadrature point is no longer occupied by a Representative Volume Element (RVE) simulation; instead, it is replaced by a surrogate model which consists of a system of Ordinary Differential Equations (ODEs). In this way, a computationally efficient solution scheme for solving two-scale problems is obtained. This strategy is henceforth denoted NMR-FE^2. The procedure is split into two stages: the off-line stage, where the surrogate model is constructed prior to the solution of the macro-scale problem, and the on-line stage, where the surrogate model is used to solve the macro-scale problem efficiently.

5.1 Transient split of RVE problem

As a starting point for the NMR framework for solving the RVE problems efficiently, we use the same governing equations established in (4.13). Additionally, we recall the stationary and transient split according to (4.14). Due to linearity, the time-dependent "stationary" parts $\bullet^{\text{stat}}(\boldsymbol{x}, t)$ can be decomposed into linear combinations that depend explicitly on the macroscopic loading histories as noted in (4.15). Next, we turn to solving the transient part of the solution by using substitution in the original equations (4.13).

For brevity, the following RVE forms are introduced

$$m_{\square,\alpha}^{(\varphi)}(\mu_\alpha, \delta\varphi) := \frac{1}{|\Omega_\square|} \int_{\Omega_\square} z'_\alpha k_\alpha \mu_\alpha \, \delta\varphi \, \mathrm{d}\Omega, \tag{5.1a}$$

$$a_\square^{(\varphi)}(\varphi, \delta\varphi) := \frac{1}{|\Omega_\square|} \int_{\Omega_\square} \boldsymbol{\nabla}\delta\varphi \cdot \boldsymbol{\epsilon} \cdot \boldsymbol{\nabla}\varphi \, \mathrm{d}\Omega, \tag{5.1b}$$

$$m_{\square,\alpha}^{(\mu)}(\mu_\alpha, \delta\mu_\alpha) := \frac{1}{|\Omega_\square|} \int_{\Omega_{\square,\mathrm{E}}} \mu_\alpha k_\alpha \, \delta\mu_\alpha \, \mathrm{d}\Omega, \tag{5.1c}$$

$$a_{\square,\alpha}^{(\mu)}(\mu_\alpha, \delta\mu_\alpha) := \frac{1}{|\Omega_\square|} \int_{\Omega_{\square,\mathrm{E}}} \boldsymbol{\nabla}\delta\mu_\alpha \cdot \boldsymbol{M}_\alpha \cdot \boldsymbol{\nabla}\mu_\alpha \, \mathrm{d}\Omega, \tag{5.1d}$$

$$a_{\square,\alpha}^{(\mu,\varphi)}(\varphi, \delta\mu_\alpha) := \frac{1}{|\Omega_\square|} \int_{\Omega_{\square,\mathrm{E}}} \boldsymbol{\nabla}\delta\mu_\alpha \cdot \boldsymbol{M}_\alpha \cdot z'_\alpha \boldsymbol{\nabla}\varphi \, \mathrm{d}\Omega. \tag{5.1e}$$

Exploiting the linearity and time-transience of Eqs. (4.13a)–(4.13c), we see that we can compute $\varphi^{\mathrm{trans}}\{\{\mu_\alpha\}_{\alpha=1}^N\} = \varphi^{\mathrm{trans}} \in \mathbb{P}_0$ together with Lagrange multipliers $(\hat{\lambda}^\varphi, \lambda^\varphi) \in \mathbb{R} \times \mathbb{P}_\square^{(\varphi)}$ such that

$$-a_\square^{(\varphi)}(\varphi, \delta\varphi) - \left\langle\!\!\left\langle \lambda^{(\varphi)} [\![\delta\varphi]\!]_\square \right\rangle\!\!\right\rangle_\square - \hat{\lambda}^{(\varphi)} \left\langle \delta\varphi \right\rangle_\square = -\sum_\alpha m_{\square,\alpha}^{(\varphi)}(\mu_\alpha^{\mathrm{trans}}, \delta\varphi)$$

$$\forall\delta\varphi \in \mathbb{P}_\square, \tag{5.2a}$$

$$-\left\langle\!\!\left\langle \delta\lambda^{(\varphi)} [\![\varphi_\alpha]\!]_\square \right\rangle\!\!\right\rangle_\square = 0$$

$$\forall\delta\lambda^{(\varphi)} \in \mathbb{T}_\square^{(\varphi)}, \tag{5.2b}$$

$$-\delta\hat{\lambda}^{(\varphi)} \left\langle \varphi_a \right\rangle_\square = 0$$

$$\forall\delta\hat{\lambda}^{(\varphi)} \in \mathbb{R}. \tag{5.2c}$$

This problem follows directly by insertion of $\varphi = \varphi^{\mathrm{stat}} + \varphi^{\mathrm{trans}}$ and $\mu_\alpha = \mu_\alpha^{\mathrm{stat}} + \mu_\alpha^{\mathrm{trans}}$, while utilizing the corresponding stationary relations.

Furthermore, we note that for a high dimension of $\{\mathbb{M}_{\square,\alpha}\}_{\alpha=1}^N$, or even worse, for the continuous case, the computation of $\varphi^{\mathrm{trans}}\{\{\mu_\alpha^{\mathrm{trans}}\}_{\alpha=1}^N\}$ is intractable in practice. However, as part of the reduced order model, this limitation will be alleviated by introducing low dimensional approximation spaces $\mathbb{M}_{\square,R,\alpha}$.

Assuming that we have the implicit relations $\varphi^{\text{trans}}\{\{\mu_\alpha^{\text{trans}}\}_{\alpha=1}^N\}$ at hand, we can solve for the transient parts μ_a^{trans} together with the Lagrange multipliers such that

$$m_{\square,\alpha}^{(\mu)}(\partial_t\mu_\alpha^{\text{trans}},\delta\mu_\alpha) + a_{\square,\alpha}^{(\mu)}(\mu_\alpha^{\text{trans}},\delta\mu_\alpha) + a_{\square,\alpha}^{(\mu\varphi)}(\varphi\{\{\mu_\beta^{\text{trans}}\}_{\alpha=1}^N\},\delta\mu_\alpha)$$

$$+\phi\left\langle\left\langle\lambda_\alpha^{(\mu)}[\![\delta\mu_\alpha]\!]_\square\right\rangle\right\rangle_{\square,\text{E}} - \hat\lambda_\alpha^{(\mu)}\,\phi\langle\delta\mu_\alpha\rangle_{\square,\text{E}} = -m_{\square,\alpha}^{(\mu)}(\partial_t\mu_\alpha^{\text{stat}},\delta\mu_\alpha)$$

$$\forall\delta\mu_\alpha\in\mathbb{M}_{\square,\alpha}, \tag{5.3a}$$

$$\phi\left\langle\left\langle\delta\lambda_\alpha^{(\mu)}[\![\mu_\alpha^{\text{trans}}]\!]_\square\right\rangle\right\rangle_{\square,\text{E}} = 0$$

$$\forall\delta\lambda_\alpha^{(\mu)}\in\mathbb{T}_\square^{(\mu)}, \tag{5.3b}$$

$$-\delta\hat\lambda_\alpha^{(\mu)}\,\phi\langle\mu_\alpha^{\text{trans}}\rangle_{\square,\text{E}} = 0$$

$$\forall\delta\hat\lambda_\alpha^{(\mu)}\in\mathbb{R}. \tag{5.3c}$$

In what follows, we shall introduce a reduced order approximation $\mu^{\text{trans}}\approx\mu_R^{\text{trans}}$. This will allow for (i) the explicit computation of the low dimensional mapping $\varphi\{\{\mu_{\alpha,R}^{\text{trans}}\}_{\alpha=1}^N\}$ from (5.2), and (ii) Galerkin scheme for the reduced problem corresponding to (5.3).

5.2 Generation of POD modes: Chemical potential

The core of the surrogate model is the adoption of a reduced basis for the chemical potential field. Here, we introduce the low dimensional spaces $\mathbb{M}_{\square,R,\alpha}=\text{span}\{\hat\mu_{\alpha,a}\}_{a=1}^{M_{R,\alpha}}$ and seek approximation of the transient fields on the form

$$\mu_\alpha^{\text{trans}}(\boldsymbol{x},t)\approx\mu_{\alpha,\text{R}}^{\text{trans}}(\boldsymbol{x},t):=\sum_{a=1}^{M_{\text{R},\alpha}^{(\mu)}}\hat\mu_{\alpha,a}(\boldsymbol{x})\xi_{\alpha,a}^{(\mu)}(t)\in\mathbb{M}_{\square,\alpha,\text{R}}^0. \tag{5.4}$$

Here, $\{\hat\mu_{\alpha_\alpha}\}_{a=1}^{M_{\alpha,a}}$ are a set of suitable basis functions for species α, and $\mathbb{M}_{\square,a}$ is the number of these modes (typically much smaller than the dimension of the underlying FE-discretization.)

As a first step, full (FE) simulations of Eqs. (4.13a)–(4.13f) for selected time histories $(\bar{\boldsymbol{g}}_\phi,\bar\mu_a,\bar{\boldsymbol{g}}_\mu)$ are carried out. These simulations are referred to as training simulations. Extracting spatial snapshots $\mu_\alpha^{\text{trans}}=\mu_\alpha-\mu^{\text{stat}}$ at selected time instances[2] $(a=1,...,S)$ from these simulations, we use Proper Orthogonal Decomposition (POD) to extract the most important modes and use them as basis.

The chemical potential modes $\hat\mu_{\alpha,a}$ are obtained upon performing POD on the snapshot correlation matrices for all chemical species $\alpha=1,2,\ldots,N$. The snapshot correlation matrix is defined as follows

$$g_{\alpha,ab}=\langle\mu_{\alpha,a}^{\text{trans}}(\boldsymbol{x})\,\mu_{\alpha,b}^{\text{trans}}(\boldsymbol{x})\rangle_\square,\quad a,b=1,2,...,S. \tag{5.5}$$

---

[2]Here, each snapshot is indicated by a given time instance from one solution μ_α. In practice, the snapshots are typically extracted from different simulations.

Here, $\mu_{\alpha,a}^{\text{trans}}(\boldsymbol{x})$ corresponds to one of the S snapshots that are directly sampled from the transient solution $\mu_\alpha^{\text{trans}}(\boldsymbol{x}, t)$. In the next step, the snapshot correlation matrices are used to solve the eigenvalue problem

$$(g_{\alpha,ab} - \lambda\,\delta_{ab})\,v_{\alpha,b} = 0, \tag{5.6}$$

whereby the identified (orthonormal) eigenvectors $v_{\alpha,k}$ and the chemical potential snapshots $\mu_{\alpha,k}^{\text{trans}}(\boldsymbol{x})$ are used to compute the chemical potential modes as follows

$$\hat{\mu}_{\alpha,a}(\boldsymbol{x}) = \sum_{k=1}^{S} v_{\alpha,k}^{(a)}\,\mu_{\alpha,k}^{\text{trans}}(\boldsymbol{x}). \tag{5.7}$$

Here, the entries in $v_{\alpha,k}^{(a)}$ take the role of mixture coefficients in a linear combination of all transient snapshots to form each mode. By construction, the resulting chemical potential modes are orthogonal in a way such that

$$\langle \hat{\mu}_{\alpha,a}(\boldsymbol{x})\,\hat{\mu}_{\alpha,b}(\boldsymbol{x})\rangle_\square = \begin{cases} \lambda_{\alpha,a}, & \text{if } a = b, \\ 0, & \text{otherwise.} \end{cases} \tag{5.8}$$

In practice, the implementation of POD is performed using matrices, where $\boldsymbol{G}_\alpha$ is the snapshot correlation (square) matrix and the eigenvalue problem $(\boldsymbol{G}_\alpha - \lambda\,\boldsymbol{I})\,\boldsymbol{v}_\alpha = \boldsymbol{0}$ results in a rectangular matrix $\boldsymbol{V}_\alpha$ of column eigenvectors $\boldsymbol{v}_\alpha$. Finally, the chemical potential mode matrix is simply computed as $\hat{\boldsymbol{\mu}}_\alpha = \boldsymbol{\mu}_\alpha^{\text{trans}}\,\boldsymbol{V}_\alpha$, given that the snapshot vectors are stacked as column vectors in the rectangular snapshot matrix $\boldsymbol{\mu}_\alpha^{\text{trans}}$.

5.3   Identification of modes: Electric potential

In the spirit of the Nonuniform Transformation Field Analysis (NTFA) [59], we shall now compute the pertinent modes for the electric potential. Using the fact that (5.2) is time invariant and linear, we may express

$$\varphi^{\text{trans}}\{\{\mu_{\alpha,R}^{\text{trans}}\}\} = \sum_{\alpha=1}^{N} \sum_{a=1}^{M_{R,\alpha}} \hat{\varphi}_{\alpha,a}(\boldsymbol{x})\xi_{\alpha,a}(t) \tag{5.9}$$

where the modes $\hat{\varphi}_{\alpha,a} \in \mathbb{P}_\square$ together with Lagrange multipliers $\lambda^{(\varphi)}, \bar{\lambda}^{(\varphi)} \in \mathbb{T}_\square^{(\varphi)} \times \mathbb{R}$ are solved such that

$$-a^{(\varphi)}(\hat{\varphi}_{\alpha,a}, \delta\varphi) - \left\langle\!\left\langle \lambda^{(\varphi)}\, [\![\delta\varphi]\!]\right\rangle\!\right\rangle_\square - \hat{\lambda}^{(\varphi)}\,\langle\delta\varphi\rangle_\square = -m_{\square,\alpha}^{(\varphi)}(\hat{\mu}_{\alpha,a}, \delta\varphi)$$

$$\forall\delta\varphi \in \mathbb{P}_\square, \tag{5.10a}$$

$$-\left\langle\!\left\langle \delta\lambda^{(\varphi)}\, [\![\hat{\varphi}_{\alpha,a}]\!]\right\rangle\!\right\rangle_\square = 0$$

$$\forall\delta\lambda^{(\varphi)} \in \mathbb{T}_\square^{(\varphi)}, \tag{5.10b}$$

$$-\langle\hat{\varphi}_{\alpha,a}\rangle_\square\,\delta\hat{\lambda}^{(\varphi)} = 0$$

$$\forall\delta\hat{\lambda}^{(\varphi)} \in \mathbb{R}, \tag{5.10c}$$

for $a = 1, 2, \ldots, M_{R,\alpha}$ and $\alpha = 1, 2, \ldots, N$. Hence, the reduced approximation

$$\varphi_R(\boldsymbol{x}, t) = \varphi^{\text{stat}}(\boldsymbol{x}, t) + \sum_\alpha \sum_a \hat{\varphi}_{\alpha,a} \xi_{\alpha,a}(t), \tag{5.11a}$$

$$\mu_{\alpha,R}(\boldsymbol{x}, t) = \mu_\alpha^{\text{stat}}(\boldsymbol{x}, t) + \sum_a \hat{\mu}_{\alpha,a} \xi_{\alpha,a}(t), \quad \alpha = 1, ..., N, \tag{5.11b}$$

will satisfy Eqs. (4.13a)–(4.13c) exactly (up to the chosen FE-discretization).

5.4 Surrogate model

The next step is to insert the appropriate NMR-approximations into the transient problem and choosing test functions according to $\delta\mu_\alpha = \hat{\mu}_{\alpha,a}$ in (5.3a), $\delta\lambda_\alpha^{(\mu)} = \lambda_{\alpha,a}^{(\mu)}$ in (5.3b) and $\delta\hat{\lambda}_\alpha^{(\mu)} = \hat{\lambda}_{\alpha,a}^{(\mu)}$ in (5.3c):

$$\sum_{b=1}^{M_{R,\alpha}^{(\mu)}} m_{\square,\alpha}^{(\mu)}(\hat{\mu}_{\alpha,b}, \hat{\mu}_{\alpha,a}) \, \dot{\xi}_{\alpha,b}^{(\mu)} + \sum_{b=1}^{M_{R,\alpha}^{(\mu)}} a_{\square_\alpha}^{(\mu)}(\hat{\mu}_{\alpha,b}, \hat{\mu}_{\alpha,a}) \, \xi_{\alpha,b}^{(\mu)}$$

$$+ \sum_{\beta=1}^{N} \left(\sum_{b=1}^{M_{R,\alpha}^{(\mu)}} a_{\square,\alpha}^{(\mu\varphi)}(\hat{\varphi}_{\beta,b}, \hat{\mu}_{\alpha,a}) \, \xi_{\beta,b}^{(\mu)} \right) + \sum_{b=1}^{M_{R,\alpha}^{(\mu)}} \phi \left\langle\!\left\langle \lambda_{\alpha,b}^{(\mu)} [\![\hat{\mu}_{\alpha,a}]\!] \right\rangle\!\right\rangle_{\square,\mathrm{E}} \xi_{\alpha,b}^{(\mu)}$$

$$- \sum_{b=1}^{M_{R,\alpha}^{(\mu)}} \hat{\lambda}_{\alpha,b}^{(\mu)} \phi \left\langle \hat{\mu}_{\alpha,a} \right\rangle_{\square,\mathrm{E}} \xi_{\alpha,b}^{(\mu)} = -m_\square^{(\mu)}(\partial_t \mu_\alpha^{\text{stat}}, \hat{\mu}_{\alpha,a}), \tag{5.12a}$$

$$\sum_{b=1}^{M_{R,\alpha}^{(\mu)}} \phi \left\langle\!\left\langle \lambda_{\alpha,b}^{(\mu)} [\![\hat{\mu}_{\alpha,a}]\!] \right\rangle\!\right\rangle_{\square,\mathrm{E}} \xi_{\alpha,b}^{(\mu)} = 0, \tag{5.12b}$$

$$- \sum_{b=1}^{M_{R,\alpha}^{(\mu)}} \hat{\lambda}_{\alpha,b}^{(\mu)} \phi \left\langle \hat{\mu}_{\alpha,a} \right\rangle_{\square,\mathrm{E}} \xi_{\alpha,b}^{(\mu)} = 0, \tag{5.12c}$$

for test functions $a = 1, 2, ..., M_{R,\alpha}^{(\mu)}$ and $\alpha = 1, 2, \ldots, N$. Here, it is clear that (5.12b) and (5.12c) can be eliminated upon insertion into (5.12a).

As a final step, the stationary part $\mu_\alpha^{\mathrm{stat}}$ is decomposed according to (4.14) and the system of equations takes the following form

$$\sum_{b=1}^{M_{R,\alpha}^{(\mu)}} m_{\square,\alpha}^{(\mu)}(\hat{\mu}_{\alpha,b}, \hat{\mu}_{\alpha,a}) \dot{\xi}_{\alpha,b}^{(\mu)} + \sum_{b=1}^{M_{R,\alpha}^{(\mu)}} a_{\square,\alpha}^{(\mu)}(\hat{\mu}_{\alpha,b}, \hat{\mu}_{\alpha,a}) \xi_{\alpha,b}^{(\mu)}$$

$$+\sum_{\beta=1}^{N} \left(\sum_{b=1}^{M_{R,\alpha}^{(\mu)}} a_{\square,\alpha}^{(\mu\varphi)}(\hat{\varphi}_{\beta,b}, \hat{\mu}_{\alpha,a}) \xi_{\beta,b}^{(\mu)} \right) = -m_{\square,\alpha}^{(\mu)}(\mu_{\alpha,\bar{\varphi}}, \hat{\mu}_{\alpha,a}) \, \dot{\varphi}(t)$$

$$-m_{\square,\alpha}^{(\mu)}(\boldsymbol{\mu}_{\alpha,\bar{g}^\varphi}, \hat{\mu}_{\alpha,a}) \cdot \dot{\boldsymbol{g}}^\varphi(t) - \sum_{\beta=1}^{N} m_{\square,\alpha}^{(\mu)}(\mu_{\alpha,\bar{\mu}_\beta}, \hat{\mu}_{\alpha,a}) \, \dot{\mu}_\beta(t)$$

$$-\sum_{\beta=1}^{N} m_{\square,\alpha}^{(\mu)}(\boldsymbol{\mu}_{\alpha,\bar{g}_\beta^\mu}, \hat{\mu}_{\alpha,a}) \cdot \dot{\boldsymbol{g}}_\beta^\mu(t), \qquad (5.13)$$

for test functions $a = 1, 2, ..., M_{R,\alpha}^{(\mu)}$ and $\alpha = 1, 2, \ldots, N$.

Here, only Li-ions (Li$^+$) and the corresponding anion (X$^-$) are considered; the explicit matrix format becomes as follows

$$\underline{\underline{M}}_{\mathrm{Li,Li}} \dot{\underline{\xi}}_{\mathrm{Li}} + \underline{\underline{K}}_{\mathrm{Li,Li}} \underline{\xi}_{\mathrm{Li}} + \underline{\underline{K}}_{\mathrm{Li,X}} \underline{\xi}_{\mathrm{X}} = \underline{f}_{\mathrm{Li},\bar{\varphi}} \, \dot{\varphi}(t) + \underline{\underline{f}}_{\mathrm{Li},\bar{g}^\varphi} \cdot \dot{\underline{g}}^\varphi(t)$$

$$+\underline{f}_{\mathrm{Li},\bar{\mu}_{\mathrm{Li}}} \, \dot{\mu}_{\mathrm{Li}}(t) + \underline{\underline{f}}_{\mathrm{Li},\bar{g}_{\mathrm{Li}}^\mu} \cdot \dot{\underline{g}}_{\mathrm{Li}}^\mu(t)$$

$$+\underline{f}_{\mathrm{Li},\bar{\mu}_{\mathrm{X}}} \, \dot{\mu}_{\mathrm{X}}(t) + \underline{\underline{f}}_{\mathrm{Li},\bar{g}_{\mathrm{X}}^\mu} \cdot \dot{\underline{g}}_{\mathrm{X}}^\mu(t), \qquad (5.14a)$$

$$\underline{\underline{M}}_{\mathrm{X,X}} \dot{\underline{\xi}}_{\mathrm{X}} + \underline{\underline{K}}_{\mathrm{X,Li}} \underline{\xi}_{\mathrm{Li}} + \underline{\underline{K}}_{\mathrm{X,X}} \underline{\xi}_{\mathrm{X}} = \underline{f}_{\mathrm{X},\bar{\varphi}} \, \dot{\varphi}(t) + \underline{\underline{f}}_{\mathrm{X},\bar{g}^\varphi} \cdot \dot{\underline{g}}^\varphi(t)$$

$$+\underline{f}_{\mathrm{X},\bar{\mu}_{\mathrm{Li}}} \, \dot{\mu}_{\mathrm{Li}}(t) + \underline{\underline{f}}_{\mathrm{X},\bar{g}_{\mathrm{Li}}^\mu} \cdot \dot{\underline{g}}_{\mathrm{Li}}^\mu(t)$$

$$+\underline{f}_{\mathrm{X},\bar{\mu}_{\mathrm{X}}} \, \dot{\mu}_{\mathrm{X}}(t) + \underline{\underline{f}}_{\mathrm{X},\bar{g}_{\mathrm{X}}^\mu} \cdot \dot{\underline{g}}_{\mathrm{X}}^\mu(t). \qquad (5.14b)$$

In condensed matrix form, the surrogate model becomes

$$\begin{bmatrix} \underline{\underline{M}}_{\mathrm{Li,Li}} & \underline{\underline{0}} \\ \underline{\underline{0}} & \underline{\underline{M}}_{\mathrm{X,X}} \end{bmatrix} \begin{bmatrix} \dot{\underline{\xi}}_{\mathrm{Li}} \\ \dot{\underline{\xi}}_{\mathrm{X}} \end{bmatrix} + \begin{bmatrix} \underline{\underline{K}}_{\mathrm{Li,Li}} & \underline{\underline{K}}_{\mathrm{Li,X}} \\ \underline{\underline{K}}_{\mathrm{X,Li}} & \underline{\underline{K}}_{\mathrm{X,X}} \end{bmatrix} \begin{bmatrix} \underline{\xi}_{\mathrm{Li}} \\ \underline{\xi}_{\mathrm{X}} \end{bmatrix} = \begin{bmatrix} \underline{f}_{\mathrm{Li}} \\ \underline{f}_{\mathrm{X}} \end{bmatrix}. \qquad (5.15)$$

With the surrogate model in hand, we can now define the approximate effective fluxes directly as a function of macro-scale data and activity coefficients. This is achieved upon inserting $\varphi = \varphi^{\text{stat}} + \varphi^{\text{trans}}$ and $\mu_\alpha = \mu_\alpha^{\text{stat}} + \mu_\alpha^{\text{trans}}$ from (4.15) and (5.4). Repeating this for all the effective fluxes related to (4.12) results in constitutive relations that can be used in the NMR-FE^2 framework. For illustration, the effective electric flux density required for NMR-FE^2 is formulated as follows

$$
\begin{aligned}
\bar{\boldsymbol{d}} \approx -\langle \boldsymbol{\epsilon}[\boldsymbol{\nabla} \otimes \boldsymbol{\varphi}_{\bar{g}^\varphi}]\rangle_\square \cdot \bar{\boldsymbol{g}}^\varphi - \sum_{\alpha=1}^{N} \left(\langle \boldsymbol{\epsilon}\boldsymbol{\nabla}\varphi_{\bar{\mu}_\alpha}\rangle_\square \, \bar{\mu}_\alpha + \langle \boldsymbol{\epsilon}\boldsymbol{\nabla} \otimes \boldsymbol{\varphi}_{\bar{g}_\alpha^\mu}\rangle_\square \cdot \bar{\boldsymbol{g}}_\alpha^\mu \right) \\
- \sum_{\alpha}^{N} \left[\sum_{a}^{M_{R,\alpha}} \langle \boldsymbol{\epsilon}\boldsymbol{\nabla}\hat{\varphi}_{\alpha,a}\rangle_\square \, \xi_{\alpha,a}^{(\mu)} \right],
\end{aligned}
\tag{5.16a}
$$

where $\bar{\boldsymbol{g}}^\varphi(t)$, $\bar{\mu}_\alpha(t)$ and $\bar{\boldsymbol{g}}_\alpha^\mu(t)$ are known macro-scale data, and $\xi_{\alpha,a}^{(\mu)}$ are activity coefficients related to the surrogate model. Remaining effective fluxes, required for NMR-FE^2, are left out for brevity.

With these relations established, we now have everything necessary to utilize the surrogate model for efficient fully transient two-scale simulations. This strategy is pursued in **Paper C**.

6 Summary of included papers

Paper A

V. Tu, L.E. Asp, N. Shirshova, F. Larsson, K. Runesson, R. Jänicke
Multifunctional Materials, vol. 3, 2020, 025001
Performance of bicontinuous structural electrolytes

In this paper, we study the multifunctional performance of various SBE microstructures by performing virtual material testing on numerically generated artificial representative volume elements (RVE). We attempt to generate some classes of periodic and bicontinuous microstructures that seem to resemble real structural electrolytes. Most of the generation techniques involve tampering with various boundary value problems to obtain solution fields that can be converted to meshable solids. The generated microstructure classes are denoted (i) bead structures, (ii) trabecular structures, (iii) imperfect trabecular structures, and (iv) inverted microstructures.

In the next step, virtual material testing is exploited to compute effective material properties. More specifically, the multifunctional performance of artificial RVEs is evaluated in terms of the elastic stiffness and ionic conductivity. The effective elastic stiffness is computed by homogenizing the sub-scale RVE problem based on linear elasticity. Here, we make the assumption that the pore pressure in the SBE can be neglected. The effective ionic conductivity is obtained upon homogenizing the sub-scale RVE problem based on linear stationary Fickian diffusion.

Upon comparing the multifunctional performance of various artificial RVEs, we identify that the trabecular structures and imperfect trabecular structures perform better than the bead structures.

Paper B

V. Tu, F. Larsson, K. Runesson, R. Jänicke
European Journal of Mechanics - A/Solids 98 (2023), 104901
Variationally consistent homogenization of electrochemical ion transport in a porous structural battery electrolyte

This paper covers the development of a multi-scale modeling framework for electrochemically coupled ion transport in SBEs. Unlike classical battery modeling, we avoid the so-called electroneutrality assumption and instead properly resolve the electric field by coupling Gauss' law with mass conservation of chemical species. After establishing the governing equations, we exploit Variationally Consistent Homogenization (VCH) to obtain a two-scale model. Upon formulating the macro-scale problem, we are able to reveal higher order non-standard conservation terms due to the VCH approach.

Numerical investigations of the sub-scale RVE problem show that the micro-transient effects, for length scales relevant to the studied application, are negligible. Therefore, we propose the assumption of micro-stationarity; this opens up for the possibility to devise

a numerically efficient two-scale solution scheme based on a priori upscaling. Finally, the paper concludes with computational results for a 2D macro-scale problem based on precomputed effective fluxes from a bicontinuous 3D RVE. Here, we are able to provoke effects of net charge accumulation, which would not be captured upon adopting the classical electroneutrality assumption.

Paper C

V. Tu, F. Larsson, K. Runesson, R. Jänicke
To be submitted
Numerical model reduction of multi-scale electrochemical ion transport

Paper C focuses on the development of a Numerical Model Reduction (NMR) framework for multi-scale modeling of electro-chemically coupled ion transport. Applying Variationally Consistent Homogenization (VCH) on the governing equations results in a two-scale model consisting of a macro-scale and a sub-scale problem. A standard strategy to solve for two-scale problems is to use the FE^2 approach, where the macro-scale and sub-scale problems are solved concurrently in a nested fashion. However, this method is computationally expensive. As an alternative approach, we exploit NMR by training a surrogate model that replaces the sub-scale RVE simulations. The training consist of performing Proper Orthogonal Decomposition (POD) on snapshots of the primary fields. The end result is a surrogate model that consists of a system of Ordinary Differential Equations (ODEs). The approach of replacing RVE computations with ODE computations leads to a computationally efficient solution scheme for solving two-scale problems. The procedure is split into two stages: the off-line stage, where the surrogate model is constructed prior to the solution of the macro-scale problem, and the on-line stage, where the surrogate model is used to solve the macro-scale problem efficiently. To demonstrate the efficacy of this framework, we conclude the paper with a numerical example on a two-scale problem consisting of a 2D RVE and a 2D macro-scale domain.

Paper D

V. Tu, F. Larsson, K. Runesson, R. Jänicke
To be submitted
Deformation-dependent ionic transport in Structural Battery Electrolytes

In this paper, we consider ionic transport in a Structural Battery Electrolyte (SBE) subjected to large deformations. The SBE is a porous bicontinuous microstructure consisting of a solid (polymer) skeleton, and pores filled with a liquid electrolyte. Upon applying mechanical loads on the SBE, the pore space changes and affects the effective mobility. Hence, computational homogenization and 3D RVEs are used to compute the deformation-dependent effective mobility via direct upscaling. We first solve the RVE-problem for the mechanical (equilibrium) problem under macro-scale deformation control, while employing Neo-Hooke hyperelasticity for the fine-scale modeling of the solid

skeleton. In the subsequent step, we model ionic transport by assuming standard diffusion with a Fickian constitutive relation and a constant mobility in the deformed setting. Pull-back to the undeformed configuration then gives the pertinent deformation-dependent mobility for the fine-scale model. Finally, we apply computational homogenization to obtain the effective mobility pertaining to the macro-scale chemical potential gradient. The numerical results show that when a compressive macro-scale loading is applied, then the pore volume is reduced. This in turn leads to a smaller effective mobility. In this numerical investigation, upon compressing the RVE macroscopically by 20% strain, the effective mobility reduces by approximately 26%.

7   Conclusions and outlook

The goal of this thesis was to develop a multi-scale and multi-physics modeling framework for Structural Battery Electrolytes (SBE). In order to achieve this, three sub-goals were identified in Section 1.2. These sub-goals have all been fulfilled to varying degrees of success. In this section, the sub-goals are revisited.

Sub-goal 1: Develop methods to numerically generate 3D Representative Volume Elements (RVEs) representing the SBE microstructures.

Paper A covers artificial Representative Volume Element (RVE) generation. By tampering with various boundary value problems (heat equation and Cahn-Hilliard equation), we were able to manipulate the solution fields to resemble SEM images of real structural electrolytes. The solution fields were in turn converted into meshable solids for virtual material testing. Upon assessing multifunctional performance of the artificial RVEs, we concluded that trabecular structures and imperfect trabecular structures perform better than the bead structures. Surprisingly, the imperfect trabecular structures performed as well as the trabecular structures. Generation of the trabecular structures is based on prescribing heat sources and heat sinks on a periodic network stemming from a 3D Voronoi tessellation; hence, their microstructures are inherently slightly more controlled and idealized. However, the imperfect trabecular structures were generated by exploiting random noise distributions as initial conditions to the Cahn-Hilliard equation. Owing to the stochastic nature of this method, the imperfect trabecular structures have been seen to contain dead-end channels as well as unconnected pores. Currently, the RVEs are only enforced to be bicontinuous and periodic; additionally, the porosity of the microstructure can only be controlled to a certain degree. Hence, in future work on **Paper A** related to this sub-goal, the priority will be on improving the RVE generation technique with respect to microstructural descriptors.

Sub-goal 2: Use virtual material tests to assess the performance of various SBE microstructures under different conditions.

Paper A concluded with virtual material testing, where the effective properties were computed via computational homogenization for numerically generated artificial RVEs. For each RVE, we computed the effective elastic stiffness and the effective ionic conductivity. Using these metrics, we could draw conclusions about the multifunctional performance of each RVE. These numerically predicted results were then compared to experimental data of real structural electrolytes. Unsurprisingly, there was a significant discrepancy between the numerical results and the experimental measurements. One explanation could be that the experimental data was extracted from structural electrolytes that contained ionic liquids (supercapacitor application) instead of organic electrolytes (battery application). Furthermore, the virtual material testing of mechanical and transport properties was performed using the simplest possible approach of assuming linear elasticity and Fick's law, respectively. In particular, using Fick's law (i.e. dilute solution theory) for ionic liquids is a significant simplification. While Fickian diffusion models are often used to

predict the transport of Li-ions in binary solutions (organic electrolyte), they can not be used to model ion transport in ionic liquids. An example of an organic liquid based binary electrolyte is $LiPF_6$, which contains the ions Li^+ and PF_6^-. However, the ionic liquid used in the experimental data is a mixture of LiTFSI (Li-cation and TFSI-anion) and EMIM-TFSI (EMIM-cation and TFSI-anion), i.e. a so-called ternary system. It has been proposed that such systems are suitably modeled via the Maxwell-Stefan equation which describes the mutual diffusion for a multi-component system [60], and introduces the notion of molecular friction between ions [61]. Nevertheless, the experimental results were kept in **Paper A** for comparison. Due to the idealized modeling approach of the artificial RVEs, they may serve as an upper-bound for real structural electrolytes in terms of multifunctional performance. With everything considered, future work on **Paper A** pertaining to this sub-goal consists of extending the diffusion formulation with multi-component couplings (ion interactions). Most likely, this approach will allow for more realistic numerical predictions in view of experimental validation.

The topic of effective deformation-dependent mobility was investigated in **Paper D**. Finite strain theory and Neo-Hooke hyperelasticity were assumed for the solid polymer phase of the SBE microstructure. Linear Fickian diffusion was assumed for the deformed pore (liquid electrolyte) domain. In order to prevent penetration as the pore space was deformed, the pore domain was modeled as a solid with a small fictitious stiffness. However, this assumption leads to artificial stiffening. In the first step, we solved the mechanical RVE problem. In the second step, the pore space displacement was used to simulated the deformation dependent ionic transport. Finally, the effective deformation-dependent mobility was computed using computational homogenization. This framework was demonstrated in a numerical example where the SBE was subjected to a compressive load. Numerical results showed that a 20% macro-scale compression resulted in approximately 26% reduction in effective mobility. Although the framework developed in **Paper D** properly handles large deformations in conjunction with ionic transport, a few uncertainties regarding the model assumptions still remain. The following issues need to be addressed in future work pertaining to **Paper D**: (i) implement a proper contact formulation to allow for fully collapsed pore channels, and (ii) utilize experimental data for validation to evaluate the performance of the framework.

Sub-goal 3: Develop a multi-scale modeling framework for electro-chemically coupled ion transport in SBEs. Devise numerically efficient solution schemes to solve for two-scale problems.

In **Paper B**, the focus was shifted toward multi-scale modeling of electro-chemically coupled ion transport processes in SBEs. The ion transport formulation was extended from **Paper A** to include both migration and diffusion. Instead of involving Maxwell's equations, the magnetic field was assumed to vary slowly, which simplified the formulation to electrostatics. Hence, the electro-chemical ion transport could be established by coupling Gauss' law with a mass conservation law for each chemical species. Moreover, Variationally Consistent Homogenization (VCH) was exploited and a two-scale model was obtained. An efficient two-scale solution scheme was proposed for the special case of micro-stationarity. Numerical studies were performed to show that the assumption of

micro-stationarity holds true for time and length scales relevant to the studied application. Finally, the paper concluded with computational results for a 2D macro-scale problem based on precomputed effective fluxes from a bicontinuous 3D RVE. While we were able to provoke net charge accumulation effects using Gauss' law, it should be noted that the employed macro-scale boundary conditions do not correspond to a battery application due to numerous simplifications, e.g. the lacking description of the electrodes and interfaces. In order to properly trace the ions inside the electrodes, a law that describes electrode kinetics such as the Butler-Volmer equation is needed. Possible future research related to **Paper B** are as follows: (i) include a FE^2 framework for numerical validation, and (ii) perform analysis of the full structural battery.

Paper C extended the multi-scale and multi-physics framework from **Paper B** by exploiting Numerical Model Reduction (NMR). Primary RVE fields were used as training data for identifying POD modes to form a surrogate model that replaces RVE computations. This resulted in a new type of framework, denoted NMR-FE^2, which is a computationally efficient solution scheme for two-scale problems. A numerical example of applying NMR-FE^2 on a two-scale problem was provided. However, the numerical example (taken from **Paper B**) contained small micro-transients, which poorly highlights the performance of the NMR-FE^2 framework. Lastly, it was also demonstrated that a speed-up factor of up to 110 could be achieved by exploiting NMR. As a part of the conclusion, a major obstacle with NMR was identified; selecting optimal training data, training strategy and POD modes for optimal accuracy (w.r.t. computational cost) is challenging. Hence, future work related to **Paper C** are summarized as follows: (i) investigate numerical examples with large micro-transients to properly showcase the NMR-FE^2 framework, and (ii) exploit error control to enable adaptive mode selection for optimal accuracy w.r.t. computational cost.

References

[1] IEA. *Trends in electric cars*. 2024. URL: https://www.iea.org/reports/global-ev-outlook-2024/trends-in-electric-cars (visited on 07/31/2024).

[2] IEA. *Electric Vehicles*. 2024. URL: https://www.iea.org/energy-system/transport/electric-vehicles (visited on 07/31/2024).

[3] W. Li et al. A review of factors influencing consumer intentions to adopt battery electric vehicles. *Renewable and Sustainable Energy Reviews* **78** (2017), 318–328.

[4] Z. P. Cano et al. Batteries and fuel cells for emerging electric vehicle markets. *Nature Energy* **3**.4 (2018), 279–289.

[5] G. Belingardi and A. Scattina. Battery Pack and Underbody: Integration in the Structure Design for Battery Electric Vehicles—Challenges and Solutions. *Vehicles* **5**.2 (2023), 498–514.

[6] A. W. Schäfer et al. Technological, economic and environmental prospects of all-electric aircraft. *Nature Energy* **4**.2 (2019), 160–166.

[7] L. E. Asp and E. S. Greenhalgh. Structural power composites. *Composites Science and Technology* **101** (2014), 41–61.

[8] L. E. Asp et al. Structural battery composites: a review. *Functional Composites and Structures* **1**.4 (2019), 042001.

[9] R. Kanno et al. Carbon Fiber as a Negative Electrode in Lithium Secondary Cells. *Journal of The Electrochemical Society* **139**.12 (1992), 3397–3404.

[10] M. H. Kjell et al. PAN-Based Carbon Fiber Negative Electrodes for Structural Lithium-Ion Batteries. *Journal of The Electrochemical Society* **158**.12 (2011), A1455.

[11] G. Fredi et al. Graphitic microstructure and performance of carbon fibre Li-ion structural battery electrodes. *Multifunctional Materials* **1**.1 (2018), 015003.

[12] J. Hagberg et al. Lithium iron phosphate coated carbon fiber electrodes for structural lithium ion batteries. *Composites Science and Technology* **162** (2018), 235–243.

[13] K. Moyer et al. Polymer reinforced carbon fiber interfaces for high energy density structural lithium-ion batteries. *Sustainable Energy Fuels* **4** (6 2020), 2661–2668.

[14] J. S. Sanchez et al. Electrophoretic coating of LiFePO4/Graphene oxide on carbon fibers as cathode electrodes for structural lithium ion batteries. *Composites Science and Technology* **208** (2021), 108768.

[15] N. Shirshova et al. Polymerised high internal phase ionic liquid-in-oil emulsions as potential separators for lithium ion batteries. *J. Mater. Chem. A* **1** (34 2013), 9612–9619.

[16] N. Ihrner et al. Structural lithium ion battery electrolytes via reaction induced phase-separation. *J. Mater. Chem. A* **5** (48 2017), 25652–25659.

[17] L. M. Schneider et al. Bicontinuous Electrolytes via Thermally Initiated Polymerization for Structural Lithium Ion Batteries. *ACS Applied Energy Materials* **2**.6 (2019), 4362–4369.

[18] W. Johannisson, D. Zenkert, and G. Lindbergh. Model of a structural battery and its potential for system level mass savings. *Multifunctional Materials* **2**.3 (2019), 035002.

[19] Honda. *Next-generation batteries will change EVs towards a carbon-neutral society! Research on all-solid-state batteries*. 2024. URL: `https://global.honda/jp/tech/All-solid-state_battery_technology/` (visited on 08/09/2024).

[20] Nissan. *All-solid-state batteries*. 2024. URL: `https://www.nissan-global.com/EN/INNOVATION/TECHNOLOGY/ARCHIVE/ASSB/` (visited on 08/09/2024).

[21] J. Newman and W. Tiedemann. Porous-electrode theory with battery applications. *AIChE Journal* **21**.1 (1975), 25–41.

[22] M. Doyle, T. F. Fuller, and J. Newman. Modeling of Galvanostatic Charge and Discharge of the Lithium/Polymer/Insertion Cell. *Journal of The Electrochemical Society* **140**.6 (1993), 1526–1533.

[23] M. Doyle and J. Newman. The use of mathematical modeling in the design of lithium/polymer battery systems. *Electrochimica Acta* **40**.13 (1995), 2191–2196.

[24] E. Samson et al. Modelling ion diffusion mechanisms in porous media. *International Journal for Numerical Methods in Engineering* **46**.12 (1999), 2043–2060.

[25] D. Danilov and P. Notten. Mathematical modelling of ionic transport in the electrolyte of Li-ion batteries. *Electrochimica Acta* **53**.17 (2008), 5569–5578.

[26] R. G. C. Edmund J. F. Dickinson Juan G. Limon-Petersen. The electroneutrality approximation in electrochemistry. *Journal of Solid State Electrochemistry* **15**.7 (2011), 1335–1345.

[27] G. Bauer, V. Gravemeier, and W. A. Wall. A stabilized finite element method for the numerical simulation of multi-ion transport in electrochemical systems. *Computer Methods in Applied Mechanics and Engineering* **223-224** (2012), 199–210.

[28] A. Salvadori, E. Bosco, and D. Grazioli. A computational homogenization approach for Li-ion battery cells: Part 1 – formulation. *Journal of the Mechanics and Physics of Solids* **65** (2014), 114–137.

[29] A. Salvadori, D. Grazioli, and M. Geers. Governing equations for a two-scale analysis of Li-ion battery cells. *International Journal of Solids and Structures* **59** (2015), 90–109.

[30] J. Xu, G. Lindbergh, and J. Varna. Multiphysics modeling of mechanical and electrochemical phenomena in structural composites for energy storage: Single carbon fiber micro-battery. *Journal of Reinforced Plastics and Composites* **37**.10 (2018), 701–715.

[31] D. Carlstedt et al. Electro-chemo-mechanically coupled computational modelling of structural batteries. *Multifunctional Materials* **3**.4 (2020), 045002.

[32] D. Carlstedt et al. Computational modelling of structural batteries accounting for stress-assisted convection in the electrolyte. *International Journal of Solids and Structures* **238** (2022), 111343.

[33] D. Carlstedt et al. On the coupled thermo–electro–chemo–mechanical performance of structural batteries with emphasis on thermal effects. *European Journal of Mechanics - A/Solids* **94** (2022), 104586.

[34] D. Grazioli, M. Magri, and A. Salvadori. Computational modeling of Li-ion batteries. *Computational Mechanics* **58** (2016), 889–909.

[35] C. Larsson et al. Effects of lithium insertion induced swelling of a structural battery negative electrode. *Composites Science and Technology* **244** (2023), 110299.

[36] R. Hill. Elastic properties of reinforced solids: Some theoretical principles. *Journal of the Mechanics and Physics of Solids* **11**.5 (1963), 357–372.

[37] S. Bargmann et al. Generation of 3D representative volume elements for heterogeneous materials: A review. *Prog. Mater. Sci.* **96** (2018), pp. 322–384.

[38] C. Soyarslan et al. 3D stochastic bicontinuous microstructures: Generation, topology and elasticity. *Acta Mater.* **149** (2018), pp. 326–340.

[39] B. D. Lubachevsky and F. H. Stillinger. Geometric Properties of Random Disk Packings. *J. Stat. Phys.* **60** (1990), pp. 561–583.

[40] A. Donev, S. Torquato, and F. Stillinger. Neighbor list collision-driven molecular dynamics simulation for nonspherical hard particles. I. Algorithmic details. *J. Comput. Phys.* **202** (2005), pp. 737–764.

[41] C. Rycroft et al. Analysis of granular flow in a pebble-bed nuclear reactor. *Phys. Rev. E* **74** (2006), 021306.

[42] D. Carolan et al. Co-continuous polymer systems: A numerical investigation. *Comput. Mater. Sci.* **98** (2015), pp. 24–33.

[43] C. Grant. Spinodal decomposition for the Cahn-Hilliard equation. *Commun. Part. Diff. Eq.* **18** (1993), pp. 453–490.

[44] M. Geers, V. Kouznetsova, and W. Brekelmans. Multi-scale computational homogenization: Trends and challenges. *Journal of Computational and Applied Mathematics* **234**.7 (2010). Fourth International Conference on Advanced COmputational Methods in ENgineering (ACOMEN 2008), 2175–2182.

[45] C. Miehe, J. Schröder, and J. Schotte. Computational homogenization analysis in finite plasticity Simulation of texture development in polycrystalline materials. *Computer Methods in Applied Mechanics and Engineering* **171**.3 (1999), 387–418.

[46] T. I. Zohdi and P. Wriggers. *An introduction to computational micromechanics*. Springer Science & Business Media, 2008.

[47] S. Nemat-Nasser and M. Hori. *Micromechanics: overall properties of heterogeneous materials*. Elsevier, 2013.

[48] D. Klepach and T. Zohdi. Strain assisted diffusion: Modeling and simulation of deformation-dependent diffusion in composite media. *Composites Part B: Engineering* **56** (2014), 413–423.

[49] J. Voges, F. Duvigneau, and D. Juhre. On the deformation dependency of the diffusion flux in solids at large deformations. *Continuum Mechanics and Thermodynamics* **34** (2022), 829–839.

[50] J. Bonet and R. D. Wood. *Nonlinear Continuum Mechanics for Finite Element Analysis 2nd Edition*. Cambridge University Press, 2008.

[51] F. Larsson et al. Computational homogenization based on a weak format of microperiodicity for RVE-problems. *Computer Methods in Applied Mechanics and Engineering* **200**.1 (2011), 11–26.

[52] S. Duan et al. Three-dimensional reconstruction and computational analysis of a structural battery composite electrolyte. *Communications Materials* **4** (2023), 49.

[53] C. Sandstrom and F. Larsson. VARIATIONALLY CONSISTENT HOMOGENIZATION OF STOKES FLOWIN POROUS MEDIA. *International Journal for Multiscale Computational Engineering* **11**.2 (2013).

[54] J. Newman and K. Thomas-Alyea. *Electrochemical Systems*. The ECS Series of Texts and Monographs. Wiley, 2004.

[55] T. Y. Hou and X.-H. Wu. A Multiscale Finite Element Method for Elliptic Problems in Composite Materials and Porous Media. *Journal of Computational Physics* **134**.1 (1997), 169–189.

[56] E. Weinan and B. Engquist. The heterognous multiscale methods. *Communications in Mathematical Sciences* **1**.1 (2003), 87–132.

[57] T. J. Hughes et al. The variational multiscale method—a paradigm for computational mechanics. *Computer Methods in Applied Mechanics and Engineering* **166**.1 (1998). Advances in Stabilized Methods in Computational Mechanics, 3–24.

[58] F. Larsson, K. Runesson, and F. Su. Variationally consistent computational homogenization of transient heat flow. *International Journal for Numerical Methods in Engineering* **81**.13 (2010), 1659–1686.

[59] J. Michel and P. Suquet. Nonuniform transformation field analysis. *International Journal of Solids and Structures* **40**.25 (2003). Special issue in Honor of George J. Dvorak, 6937–6955.

[60] K. Yoo et al. Electrochemical Model for Ionic Liquid Electrolytes in Lithium Batteries. *Electrochimica Acta* **176** (2015), 301–310.

[61] J. Wesselingh, P. Vonk, and G. Kraaijeveld. Exploring the Maxwell-Stefan description of ion exchange. *The Chemical Engineering Journal and the Biochemical Engineering Journal* **57**.2 (1995), 75–89.